

2. TECTONIC AND THERMAL STRUCTURE OF THE MIDDLE VALLEY SEDIMENTED RIFT, NORTHERN JUAN DE FUCA RIDGE¹

Earl E. Davis² and Heiner Villinger³

ABSTRACT

Recently acquired single- and multichannel seismic reflection profiles and over 500 heat flow measurements augment SeaBeam bathymetric and SeaMARC II and I side-scan acoustic data to provide new constraints on the tectonic setting and thermal structure of the sediment-filled rift, Middle Valley, of the northern Juan de Fuca Ridge. Over most of the length of the Juan de Fuca Ridge, spreading takes place along high-standing volcanic ridges, which are broken only by relatively small axial rift grabens. Near the northern end of the ridge south of the Sovanco fracture zone intersection, the volcanic supply is diminished, probably because of the lateral heat loss at the end of the ridge and the northern migration of the ridge in the wake of the lithospheric Explorer plate. This has resulted in the formation of deep rift valleys at the spreading axis. The deepest of these, Middle Valley, has been buried syntectonically by Pleistocene turbidite sediment. Heat flow in this valley varies inversely with sediment thickness, suggesting that the sediment forms a hydrologic seal over permeable igneous crust, where efficient hydrothermal circulation maintains relatively uniform temperatures. This simple model is investigated by comparing directly the thermal regime at depth and the seismic structure of the valley. Temperatures at depth are estimated from seafloor heat flow measurements using sediment physical properties derived from multichannel seismic (MCS) velocities. Although it is transitional and poorly defined in places, the acoustically defined sediment-basement contact is estimated to be typically about 300° C. Numerous local heat flow anomalies are observed in the valley. Two are associated with known hydrothermal vents also of roughly 300° C. Another lies near the normal-fault scarp that forms the eastern boundary of the valley, where basement is exposed at the seafloor, although in general, heat flow in the vicinity of the fault is relatively low, as are estimated basement temperatures. This suggests that the fault and the exposure of basement may serve primarily as a conduit for diffuse recharge of crustal fluids. Other heat flow anomalies and associated vents or vent fields overlie buried basement edifices where the sediment cover is locally attenuated. There is no significant heat flow anomaly and apparently no hydrothermal discharge associated with the most recent (Holocene) intrusive activity in the valley. The location of hydrothermal upflow zones appears to be influenced more by permeability structure, which is inferred to be controlled primarily by basement topography and variations in sediment thickness, rather than by the location of heat sources. The generally continuous, low-permeability sediment cover allows local vents to tap large areas of high-temperature permeable crust. The 300° C hydrothermal fluid temperatures currently present in Middle Valley are low compared to those required to produce solutions of high metal concentration. The presence of base-metal sulfide deposits in the valley suggests either that the "reservoir" temperature has been higher in the past, or that the fluids that produced the deposits tapped local, and possibly deeper sources of heat.

INTRODUCTION

Sediment-covered spreading centers, although relatively rare, provide important opportunities for quantitative studies of seafloor spreading and associated submarine hydrothermal systems. The sediment can preserve a stratigraphic record of magmatic, tectonic, and thermal events associated with seafloor spreading, and provide clues to the spatial and temporal variability of these processes. A regionally continuous, relatively impermeable sediment cover conductively insulates the underlying young crust and limits the possible pathways for recharge and discharge of hydrothermal fluids. Where discharge does occur, it can be strongly focused and very large sulfide deposits can be produced. A sediment layer also provides a seafloor environment in which systematic heat flow measurements can be made in a way that is not possible in normal, sediment-free ridge crest settings.

There are three well-studied sediment-covered spreading centers in the eastern Pacific Ocean: Middle Valley on the Juan de Fuca Ridge, Escanaba Trough on the Gorda Ridge, and Guaymas Basin in the Gulf of California. The first two of these are the axial rift valleys of relatively "normal" spreading centers that are situated close enough to the continental margin of western North America to have received large quantities of turbidite sediment during the Pleistocene. The last

is a young spreading center that has developed in the wake of continental rifting between Baja California and mainland Mexico, and is covered by a mixture of terrigenous and pelagic sediments. High-temperature hydrothermal discharge and sulfide deposits have been observed and sampled at all three locations (e.g., Lonsdale and Becker, 1985; Davis, Goodfellow, et al., 1987; Koski et al., 1988). Numerous detailed geophysical studies have been carried out that define the structural and in particular the thermal setting in which these deposits have formed (e.g., Guaymas Basin: Lawver et al., 1975; Lawver and Williams, 1979; Williams et al., 1979; Lonsdale and Becker, 1985; Becker and Fisher, 1991; Fisher and Becker, in press; Middle Valley: Davis and Lister, 1977a; Davis, Goodfellow, et al., 1987; Escanaba Trough: Morton et al., 1987; Abbott et al., 1986; Davis and Becker, 1992). The results have shown that reconnaissance surveys can easily detect the large variability and the isolated highs in heat flow caused by hydrothermal activity, but that much more detailed surveys, with spacings between measurements on the order of a few hundred meters or less, are required to characterize properly the nature of heat flow variability so that clear inferences can be drawn about the associated hydrothermal processes.

In this paper we present compilations of SeaBeam bathymetry, SeaMARC II and I acoustic imagery, seismic reflection profiles, and detailed heat flow measurements collected during a series of cruises to the southern part of Middle Valley from 1983 to 1989, and discuss the implications of these data regarding the nature of hydrothermal circulation and discharge in this sedimented rift. Some of the regional data have been published previously (e.g., Karsten et al., 1986; Davis et al., 1984, 1986; Davis, Goodfellow, et al., 1987), and the details of the data acquisition can be found in those references. New data

¹ Davis, E. E., Mottl, M. J., Fisher, A. T., et al., 1992. *Proc. ODP, Init. Repts.*, 139: College Station, TX (Ocean Drilling Program).

² Pacific Geoscience Centre, Geological Survey of Canada, P.O. Box 6000, Sidney, B.C. V8L 4B2, Canada.

³ Alfred Wegener Institute, Postfach 120161, D-2850 Bremerhaven, Federal Republic of Germany.

include multichannel seismic reflection profiles and heat flow determinations; the details of acquisition and processing of these data are described in Rohr et al. (1992) and in this paper. These data, along with detailed geological and geochemical sampling (J. Franklin, W. Goodfellow, and J. Lydon, pers. comm., 1991), provided the primary background information used to design the drilling strategy for Ocean Drilling Program (ODP) Leg 139. More detailed interpretations of the hydrologic, thermal, and tectonic structure of the valley will be done using the additional constraints provided by this leg and detailed stratigraphic and structural interpretation of the available single- and multichannel seismic lines.

TECTONIC SETTING

Regional Tectonics

The Juan de Fuca Ridge is located a few hundred kilometers off the coast of western North America between the Blanco and Sovanco fracture zones (Fig. 1). Over most of its length, spreading takes place at a rate of about 60 mm/yr (full rate), and the ridge crest morphology is similar to that of other medium to fast spreading-rate ridges. Rifting takes place in small axial rift zones or grabens at the summits of linear volcanic ridges that are generally continuous along 50- to 100-km-long segments. A significant exception to the general morphology occurs at the northern end of the ridge, near the intersection of the ridge with the Sovanco fracture zone. There spreading currently takes place in three deep axial valleys (McManus et al., 1972; Barr and Chase, 1974; Davis and Lister, 1977b; Karsten et al., 1986). The combination of the basement relief and the abundant supply of turbidite sediment during the Pleistocene, primarily from Queen Charlotte Sound in the north (Fig. 1), results in the spreading axis in one of these, Middle Valley, being fully buried by sediment.

The change in ridge crest morphology is believed to be the result of diminishing magma supply near the anomalously cool fracture-zone intersection (Sleep and Biehler, 1970). The effect of the deep thermal contrast across the fracture zone in this case is probably exacerbated by the northward motion of the ridge over the asthenosphere which puts the northern end of the ridge in the wake of the Explorer plate (see Fig. 1). This inference is supported by the observation that the southern end of the ridge, which leads the adjacent Pacific plate over the asthenosphere, is magmatically robust and does not deepen significantly near the Blanco transform intersection (e.g., Crane et al., 1985).

The history of rifting and sedimentation at the northern end of the Juan de Fuca Ridge has been discussed by McManus et al. (1972), Barr and Chase (1974), Davis and Lister (1977b), and Karsten et al. (1986). Additional constraints are provided by more recently acquired magnetic data (Currie et al., 1983), SeaMARC II (12 kHz) (Davis, Currie, and Sawyer, 1987) and SeaMARC I (30 kHz) acoustic side-scan imagery, and numerous single- and multichannel seismic reflection profiles collected in the area. In detail, the recent history of this segment of the Juan de Fuca Ridge is complex. Since about 5 Ma, the motion of the Explorer plate has become increasingly independent of that of the Juan de Fuca plate (Riddihough, 1984). The northern end of the Juan de Fuca Ridge, the Sovanco transform (Cowan et al., 1986), and the Nootka fault (Hyndman, Riddihough, and Herzer, 1979), are now the components of an unstable triple junction between the Pacific, Juan de Fuca, and Explorer plates. All three boundaries are diffuse (see Figs. 1 and 2A), and their histories, particularly those of the Sovanco and Nootka fault zones, are not well constrained.

The current tectonic regime (Fig. 2A) is defined well by the bathymetry (Fig. 2B) and acoustic imagery of the area (Fig. 2C). Among the dominant features are (1) the Heck seamount chain, which intersects the ridge at a latitude of 48° 20' N, and (2) the Endeavour, West, and Middle rift valleys, which form closed depressions that lie up to 240, 540, and 80 m, respectively, below the regional 2520-m-deep level of the turbidite plain north of the area. There are no barriers blocking turbidite sediment supply to any of the valleys. Thus, during

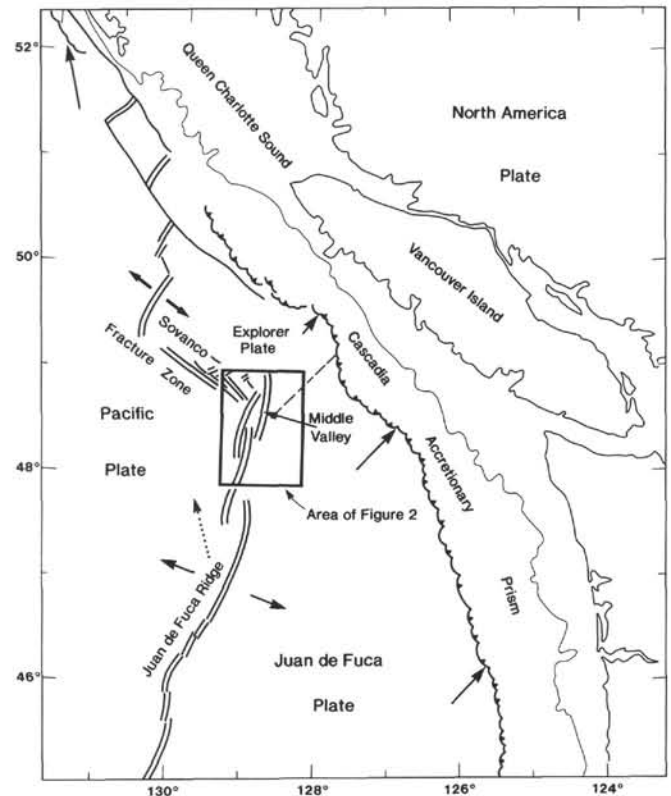


Figure 1. Location map showing the tectonic setting of the northern Juan de Fuca Ridge and the sedimented Middle Valley rift. The area included in Figure 2 is shown by the rectangular box. Solid arrows show local relative plate motion vectors; the dotted arrow shows the motion of the Juan de Fuca Ridge in an asthenospheric reference frame (Riddihough, 1983).

the Pleistocene, when sediment supply from the continental margin was high, the valleys would have been kept full. The current relief in each of the valleys must have been produced by subsidence that has occurred during the most recent interglacial period (i.e., during the last 10,000 yr), when the supply of sediment from the continental margin (e.g., Luternauer et al., 1989) and the deep-sea sedimentation rate (e.g., Al-Aasm and Blaise, 1991) were low.

West Valley

The greatest amount of subsidence during this period of time has occurred in West Valley, where rifting appears to have been initiated recently in older crust near the inferred western edge of the Brunhes magnetic chron (see Fig. 2D). It is argued below that spreading during the Brunhes Chron must have been concentrated in Middle Valley, and that relatively little total extension can have taken place in West Valley. This is not unreasonable with respect to the structure of West Valley because the time that would be required to produce the amount of extension implied by the observed subsidence is not great. Assuming that the subsidence has been produced by stretching at 58 mm/yr of a 6-km-thick crust that is half compensated by mantle replacement (in general accord with the gravity field over the valley; Lucas, 1972; Pearson, 1975), an extensional history of only 15,000 yr is implied. Roughly half of the central portion of the valley is floored by recent (post-10,000 yr) volcanics (Fig. 2C), although single- and multichannel seismic reflection data show that most of this volcanic surface represents only thin flows that rest on top of a thick sediment section (up to 650 ms two-way traveltime [TWT]; see Davis and Lister, 1977a), which in turn covers the older crust of the valley. The valley shoals and narrows to the north where it merges with the Sovanco

fracture zone, and to the south where it cuts through the young end of the Heck seamount chain and overlaps the Endeavour segment of the ridge.

Endeavour Valley

Endeavour Valley is a half-graben that contains the northernmost part of the Endeavour segment rift zone. The valley floor slopes gently down toward the base of an up to 250-m-high normal-fault scarp that forms the eastern boundary of the valley. This fault cuts an extensive volcanic surface that appears to be of relatively uniform age in both 12- and 30-kHz acoustic imagery (Davis et al., 1984; Fig. 2C). To the east of the scarp, the extrusive unit rests on top of the turbidite surface of the southern end of Middle Valley. Thus the eruption of the volcanics seen in the acoustic imagery in this area, the formation of the graben, and the more recent rifting that cuts the valley floor must have been sequential, and all must be more recent than the most recent turbidite sedimentation in the southern end of Middle Valley (i.e., probably post-Pleistocene). Currently the rift zone lies within a few kilometers of the base of the eastern valley-bounding scarp, and extends along axis with only minor offsets from the Endeavour ridge segment axial rift zone to a latitude of 48° 15' N. There it begins to curve toward the West Valley rift, cutting through the ridge that separates West Valley and Middle Valley just south of 48° 30' N, and forming a conjugate, overlapping rift pair with the rift zone of southern West Valley. This rift geometry is clearly a recent development. Before roughly 10,000 yr ago, the rift axis probably extended continuously and approximately linearly from the Endeavour segment into Middle Valley. The uplifted sedimentary "fan" or half-dome in the southern part of Middle Valley, centered at 48° 25' N, 128° 52' W (Fig. 2B), may be a consequence of the shift in the rift axis. Roughly 200 m of relief appears to have been produced at the apex, possibly by thermal or magmatic inflation. The local bathymetric slope is particularly steep on the northern side of this dome; erosional rilles, seen in SeaMARC II (Fig. 2C) and SeaMARC I acoustic side-scan imagery and in 3.5-kHz echo-sounding profiles, incise the seafloor that slopes down to the north toward the deepest part of Middle Valley.

Middle Valley

Middle Valley displays the least amount of post-Pleistocene subsidence, indicating that spreading here must have slowed considerably during the past 10,000 yr or so. The valley appears to have been the primary center of spreading until very recent times, however. This is suggested by the close colinearity of the Middle Valley and central Endeavour ridge segment axes (Fig. 2A, 2B), and to a limited degree by the position of the valley with respect to local magnetic anomalies (Fig. 2D). The western boundary of the Brunhes positive magnetic chron is complicated by the presence of the volcanic edifices of the Heck seamount chain and the Sovanco fracture zone, and the central anomaly itself is highly disrupted, probably as a result of the high temperatures within and the high degree of alteration suffered by the igneous crust beneath the sediments of both Middle Valley and West Valley (Fig. 2D) (Davis and Lister, 1977b; Levi and Riddihough, 1986). Thus, a complete, fully symmetric central magnetic chron is not present along this section of the Juan de Fuca Ridge. East of the axial region, however, the edge of the Brunhes magnetic chron, as well as older anomalies, are well defined and continuous up to a latitude of about 48° 50' N (Raff and Mason, 1961; Currie et al., 1983), indicating that the spreading history prior to a few hundred thousand years ago was relatively simple, and that a somewhat more "normal" unsedimented extrusive volcanic environment was present at the axis of spreading. The position of Middle Valley relative to the eastern edge of the Brunhes Chron provides some control on the age of the valley. The center of the valley lies roughly 17 km west of the 0-nT magnetic field anomaly contour (cf. Fig. 2B, 2D). This is within about

3 km of where the center of the Brunhes Chron would be, if crust within the Brunhes Chron had been produced at a rate of 58 mm/yr (see Fig. 3 below). A 20-km half-width of the Brunhes Chron is equivalent to that farther south along the Endeavour ridge segment. This suggests that the cessation of spreading in Middle Valley must have been very recent, and that only a minor amount of extension can have accumulated in the adjacent West Valley. As discussed above, the structure of West Valley is consistent with this observation.

Nootka Fault

The one other element that probably plays a significant role in the tectonics of the area is the Nootka fault that forms the boundary of the Explorer and Juan de Fuca plates, and intersects the north end of the Juan de Fuca Ridge to form an unstable triple junction (Hyndman, Riddihough, and Herzer, 1979; Lister, 1989). The fault is defined by a 20- to 30-km-wide zone of seismicity that extends from the northern end of the ridge to the continental margin off central Vancouver Island (Hyndman, Riddihough, and Herzer, 1979; Waldstrom and Rogers, 1990). One strand of the fault that appears in the acoustic imagery of Figure 2C (see also the foldout in the back pocket of this volume) lies directly along strike from the band of seismicity. At this location, the fault interrupts the continuity of the normal-fault block that bounds Middle Valley to the east (Fig. 2B), but not the magnetic anomalies (Fig. 2D). This provides a constraint on the amount of horizontal offset that this fault strand has experienced, probably less than a few hundred meters. Other parallel but minor disruptions of the same normal fault block are seen to the north (Fig. 2B); these may be expressions of other strands of the Nootka fault zone. If the northern part of the Juan de Fuca Ridge has migrated north past the Nootka fault intersection, as is suggested by simple plate-motion vector analysis, then the northernmost part of the ridge, including the northern part of Middle Valley, may now be spreading at the rate of the Explorer Ridge, about 40 mm/yr.

THE STUDY AREA

Tectonic Structure

The area chosen for the detailed study discussed in this paper (Fig. 4) was chosen to include a number of features seen in the SeaBeam-derived bathymetry and SeaMARC II side-scan acoustic imagery that were subsequently found to have associated hydrothermal mineralization (Davis, Goodfellow, et al., 1987; Goodfellow and Blaise, 1988). The area is situated south of where the Nootka fault zone intersects the ridge, and away from the complexities associated with the triple junction that were discussed above.

Numerous regional and detailed aspects of this part of Middle Valley are characterized by the suite of selected single- and multi-channel reflection profiles shown in Figure 3 (see also the foldout in the back pocket of this volume). The primary structural bounds of the valley are defined by the two opposed major steps of the basement surface seen 3 km west and 5 km east of the axial line (defined in caption to Fig. 3). These are inferred to have been produced by normal faulting. Along strike to the north, there is substantial bathymetric relief associated with both faults (see Fig. 2A). Within the study area, the bathymetric relief is considerably diminished along both sides of the valley. The western bounding fault becomes complicated by the recent rifting in northern Endeavour Valley, which has migrated west to form the overlapping rift with southern West Valley as discussed above. Bathymetric relief along the eastern fault diminishes to only about 50 m south of Nootka fault (Figs. 2B and 4), and there is no exposure of basement (Fig. 3).

Basement outcrops occur 6 km farther to the east (12 km east of the axial reference line of Fig. 3), where the throws on a series of normal faults exceed the thickness of sediment, locally burying basement of the footwall blocks. Surface offsets on these faults are typically 100 to 200 m, and the scarps formed are extremely steep.

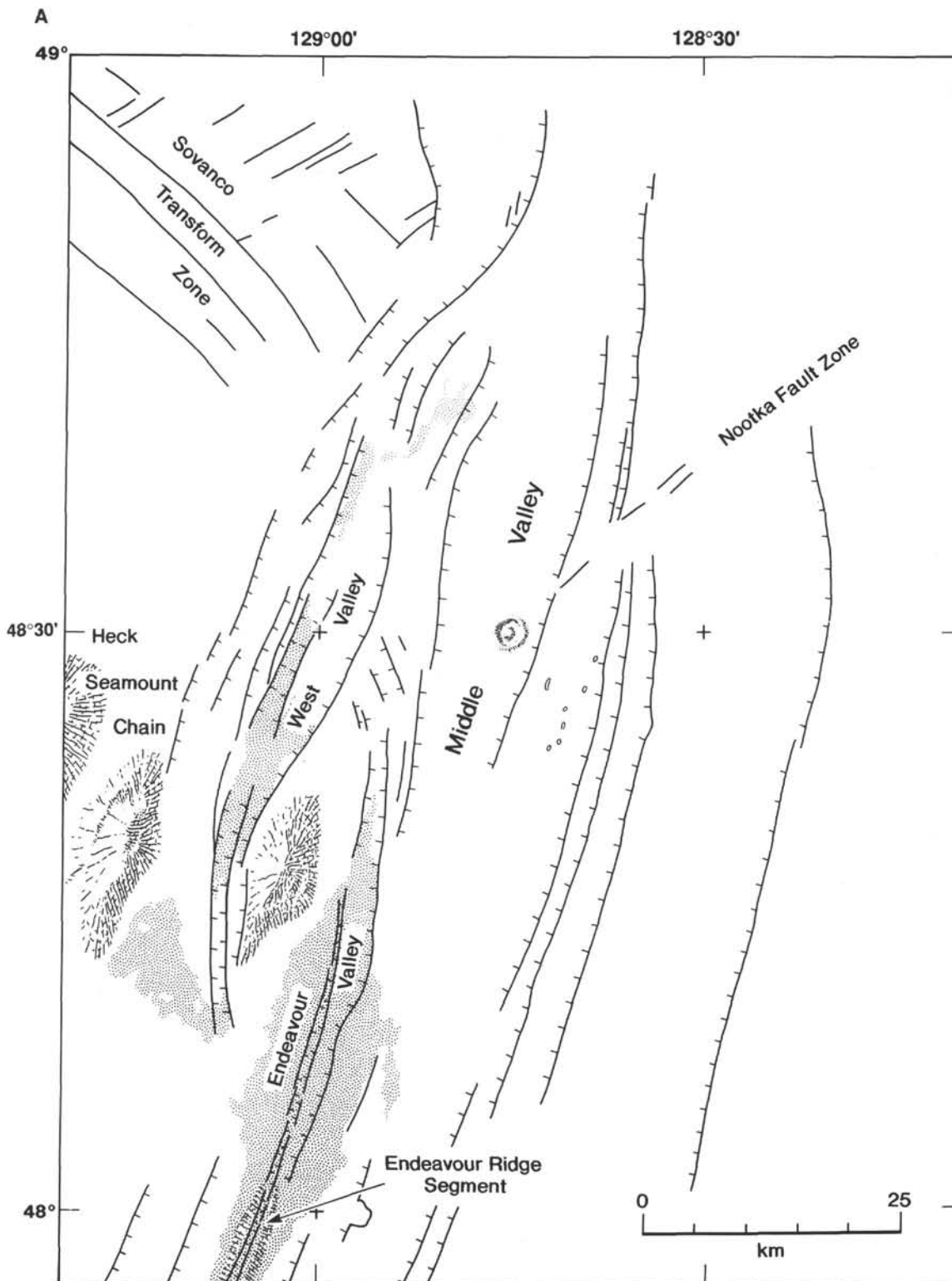


Figure 2. A. Tectonic interpretation of the area shown in (B–D), with names shown for each of the major tectonic elements in the area. Stippled areas show recent volcanic flows as inferred from the acoustic imagery in (C). B. Bathymetry of the northern Juan de Fuca Ridge, shown as contours drawn at 20-m intervals and “illuminated” from the west. The area included in Figures 3 and 9 is outlined by the rectangular box. These data and those shown in (C) are derived from Davis, Goodfellow, et al. (1987). C. 12-kHz (SeaMARC II) side-scan acoustic image mosaic of the same area as (B). Areas causing high-amplitude specular reflections or acoustic backscatter are shown dark; areas of smooth seafloor are shown light. D. Magnetic field anomaly (relative to IGRF), hand-contoured from data collected at roughly 200-m intervals along parallel tracklines oriented northeast-southwest and spaced 10 km apart. Raw data were derived from Currie et al. (1983). The 0.7-Ma Brunhes/Matuyama magnetic polarity boundary is shown by the stippling.

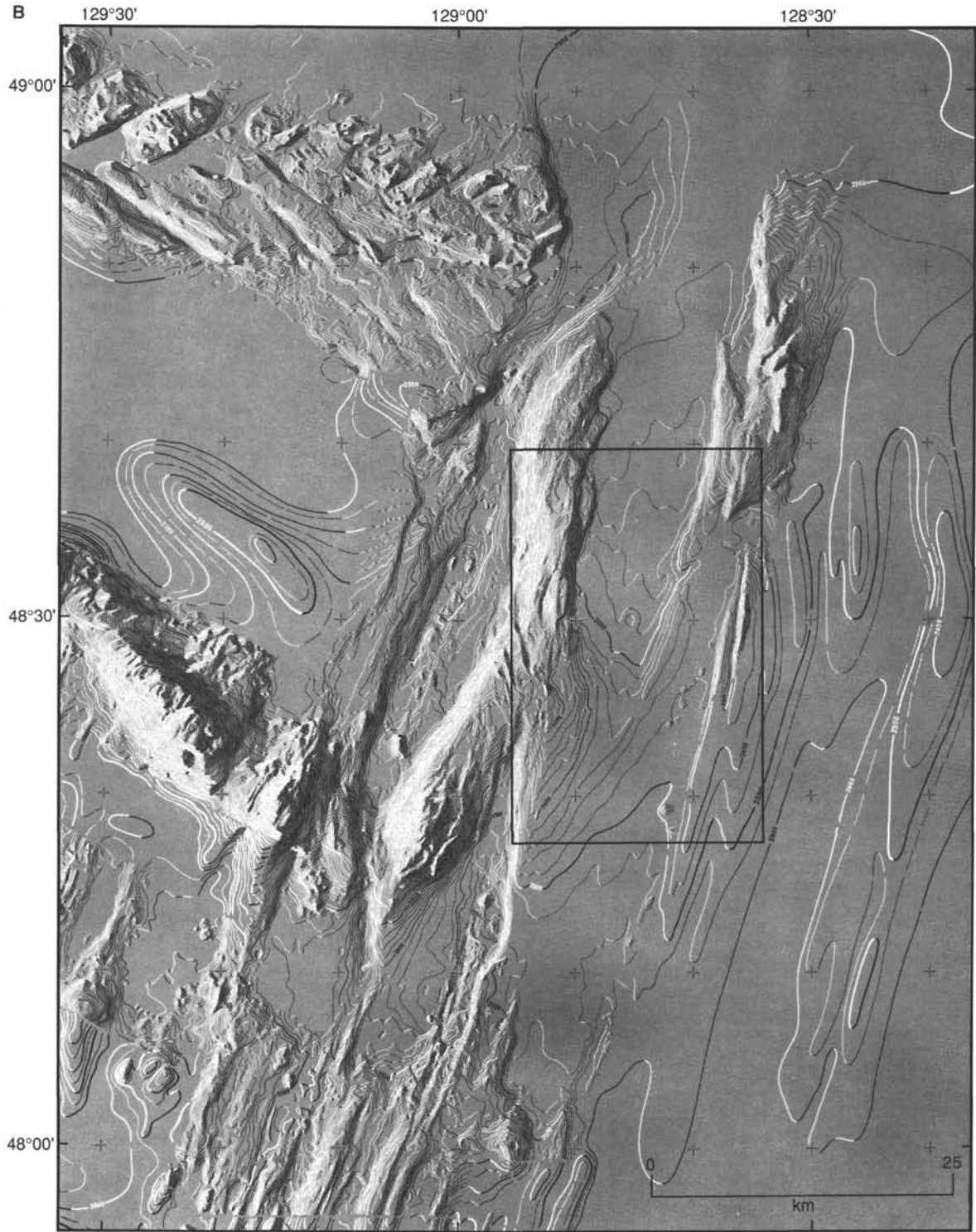


Figure 2 (continued).

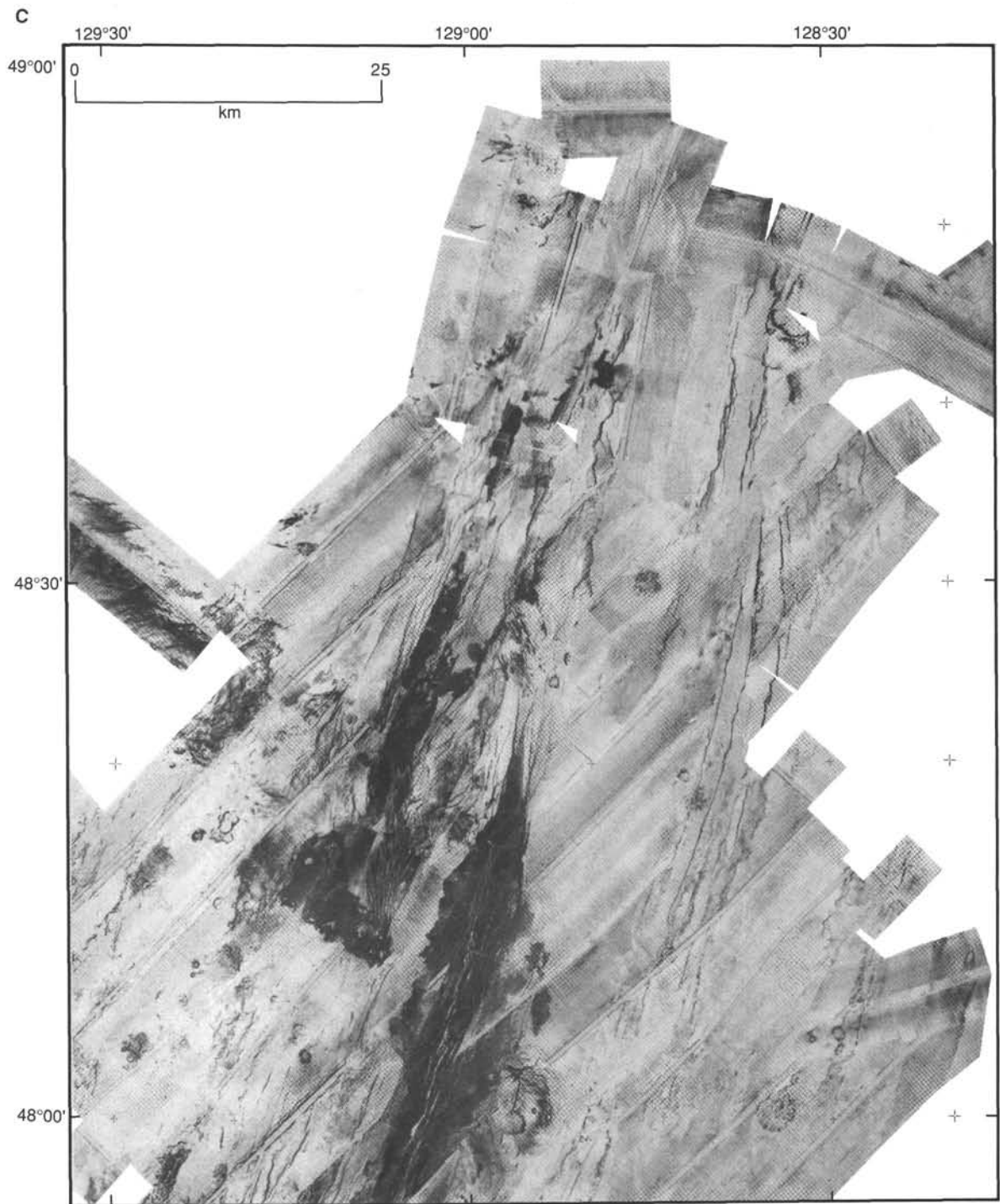


Figure 2 (continued).

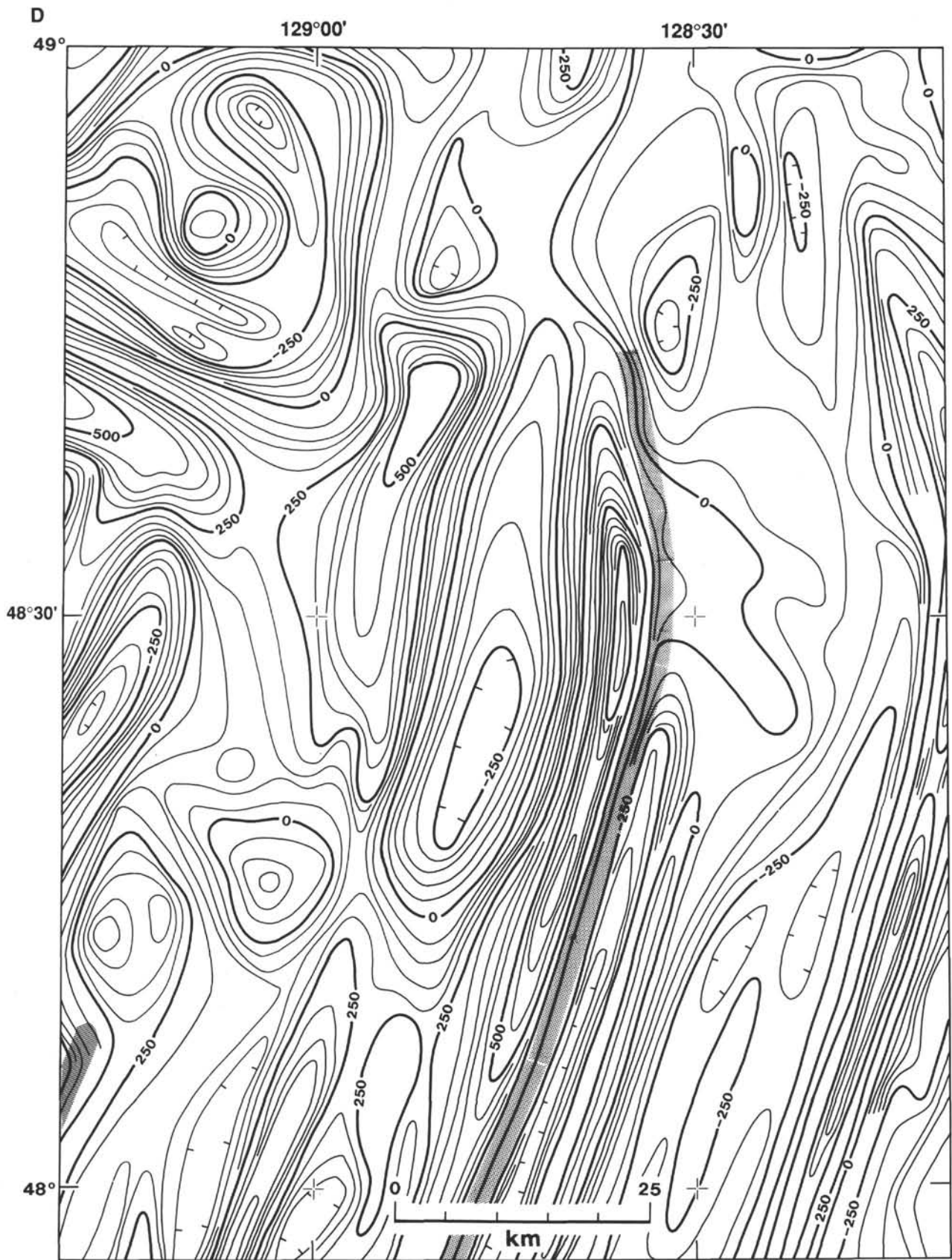


Figure 2 (continued).

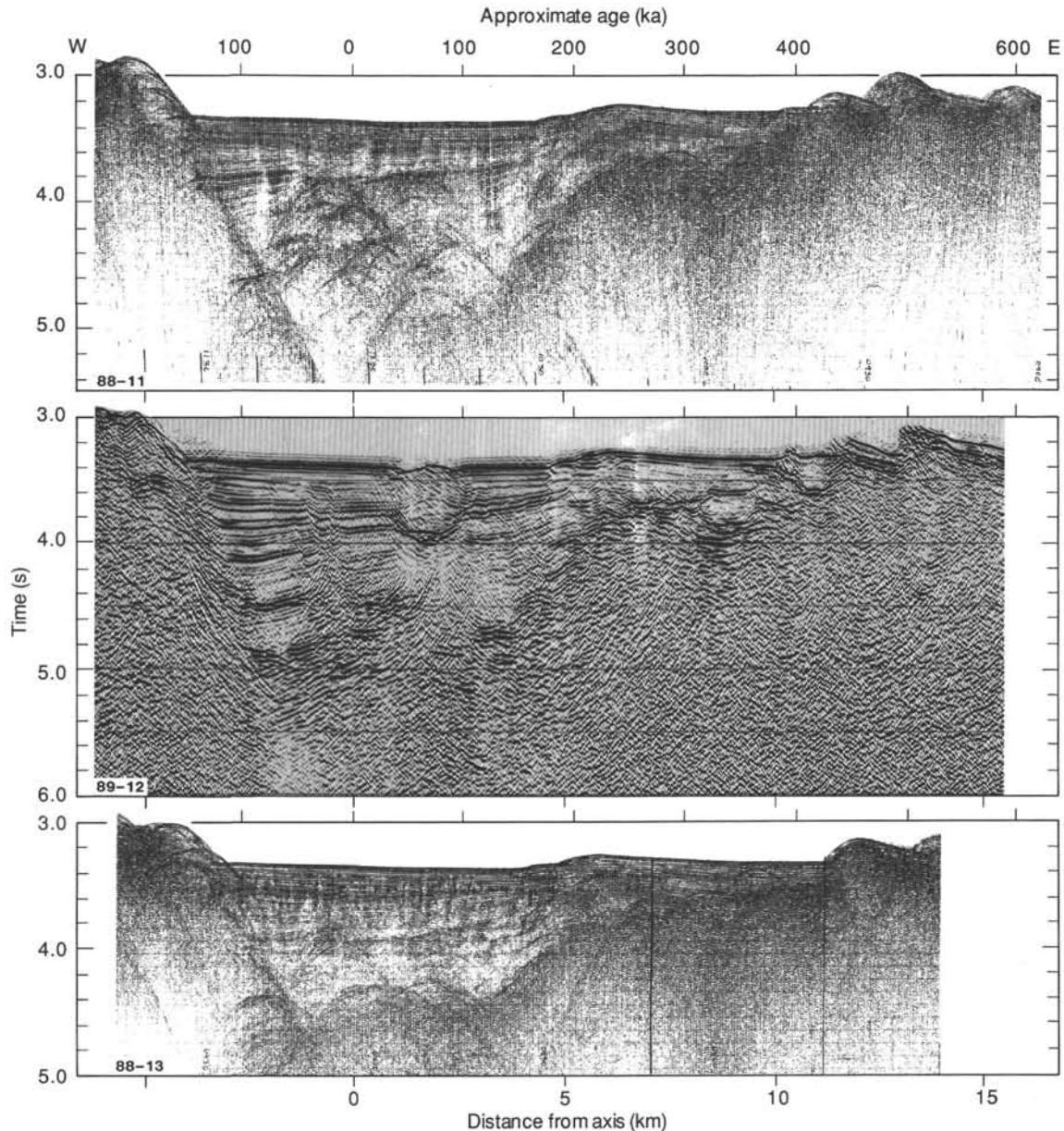


Figure 3. Selected single- and multichannel seismic reflection profiles that cross Middle Valley. Lines are nominally 2 km apart at locations shown in Figure 4. Lines 88-11, -13, and -14, and line 85-04 were completed with a single 0.65-L air gun and a single-channel receiving hydrophone array. Lines 89-12, -13, and -14 were completed with an array of 60 air guns totaling 100 L and a 3600-m-long, 144-channel hydrophone array. Other details concerning data collection and processing are given in Rohr et al. (1992). Distances along the profiles are shown as kilometers east and west of an axial reference line (kilometer zero) that is a simple projection into Middle Valley of a line striking through the central part of the Endeavour rift segment. Approximate crustal age is simply calculated from the distance from this axial line assuming a spreading rate of 29 mm/yr.

The plan-view width of these faults displayed in both 12-kHz surface-towed (SeaMARC II) and 30-kHz deep-towed (SeaMARC I) side-scan acoustic imagery, is typically less than 100 m; this width, combined with the observed throw on the faults, constrains the local seafloor slopes to being greater than about 50° .

With only minor exceptions the structure of the sediment section in Middle Valley indicates a relatively simple history. Dips of sedimentary reflectors increase with depth in a fairly uniform way, indicating either that both the rate of turbidite sedimentation and the rate of asymmetric subsidence have been constant, or more likely that the basin has been kept full as subsidence proceeded. A similar conclusion about the tectonic and sedimentary history of the valley

was made by Davis and Lister (1977b), who observed that the offsets on normal faults that cut the sediment section farther north in the valley increase uniformly with depth. These observations imply that the base level of turbidite supply is established regionally, and that the supply to the valley itself has been on average sufficient to keep pace with the subsidence. Only after the seafloor is lifted above the base level of sedimentation for a period of time can significant hiatuses develop, such as in the case of the rotated and uplifted blocks east of the valley (possibly now including the high-standing area between kilometer 5 and kilometer 12 east; Fig. 3).

The general pattern of sediment thickness variations in the valley is well defined by the seismic data. Along the bench between the

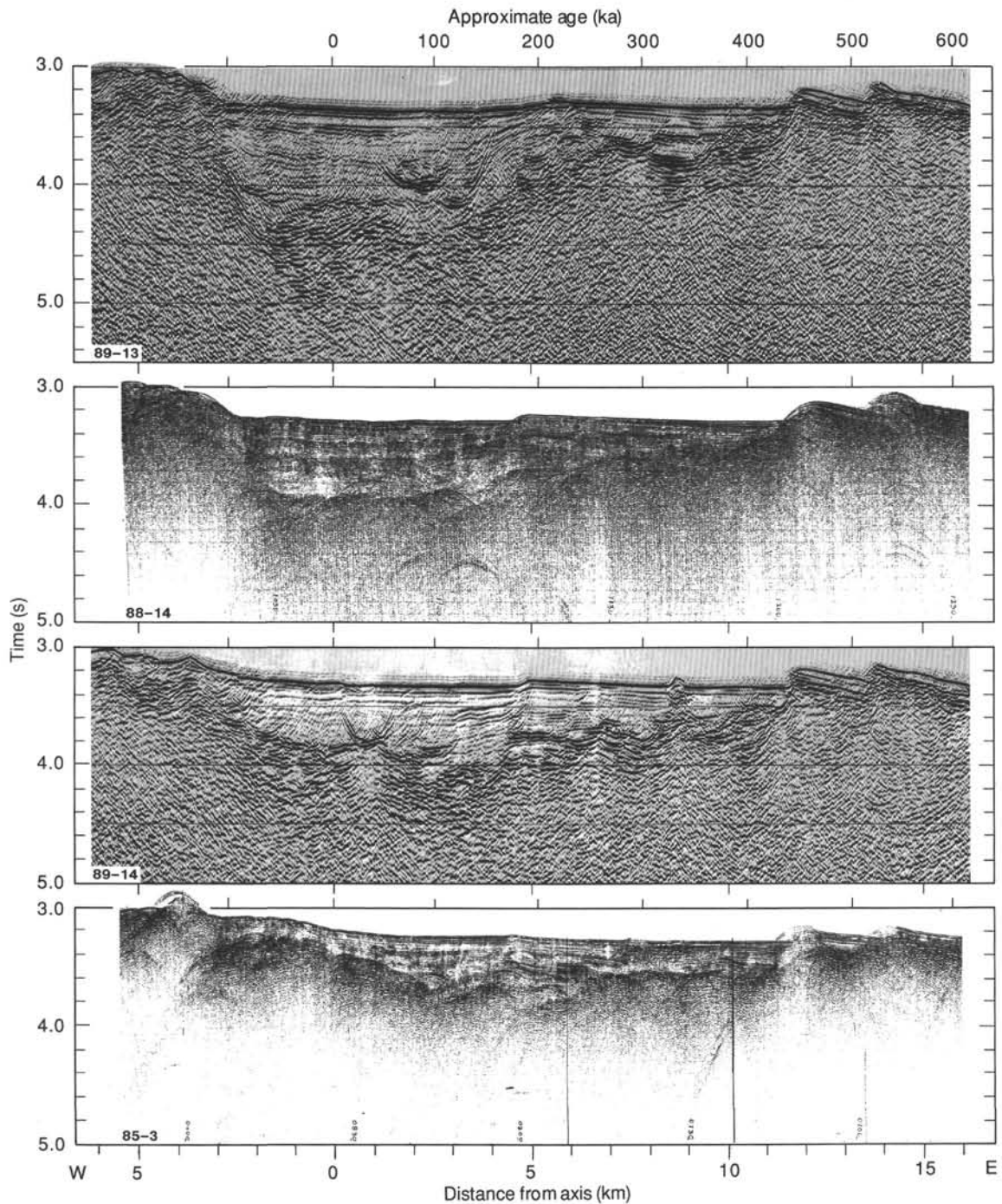


Figure 3 (continued).

eastern scarps and the buried central-rift bounding fault, basement is buried by a few hundred meters of sediment. Basement steps and dips down to the west into the central part of the rift, which has developed as a half-graben. Along the axis, basement deepens to the north, with the thickness of the overlying sediment fill ranging from a few hundred meters in the south (line 85-03) to possibly greater than 2 km in the northern part of the area (line 89-12).

Nowhere is the sediment/basement interface sharp; this is particularly evident in the multichannel profiles 89-12, 89-13, and 89-14, where numerous highly reflective, semicontinuous layers can be seen over an interval of up to 0.5 s below the highest-level "basement"

reflection. A transitional boundary is implied; the top of purely igneous crust probably grades into the sediment section through a zone of intercalated sediments and basaltic sills and flows. Comparison of adjacent single- and multichannel profiles (e.g., lines 88-13 and 88-14) shows that the higher frequency and lower capacity sources used for the single-channel lines do not image the deeper reflectors, and provide only a minimum estimate of the sediment thickness. At a few locations, isolated highly reflective layers are seen high within the sediment section (e.g., Figs. 5 and 6). These reflections are often very strong, considerably higher in amplitude than the seafloor reflection, and are also probably caused by sills or buried flows.

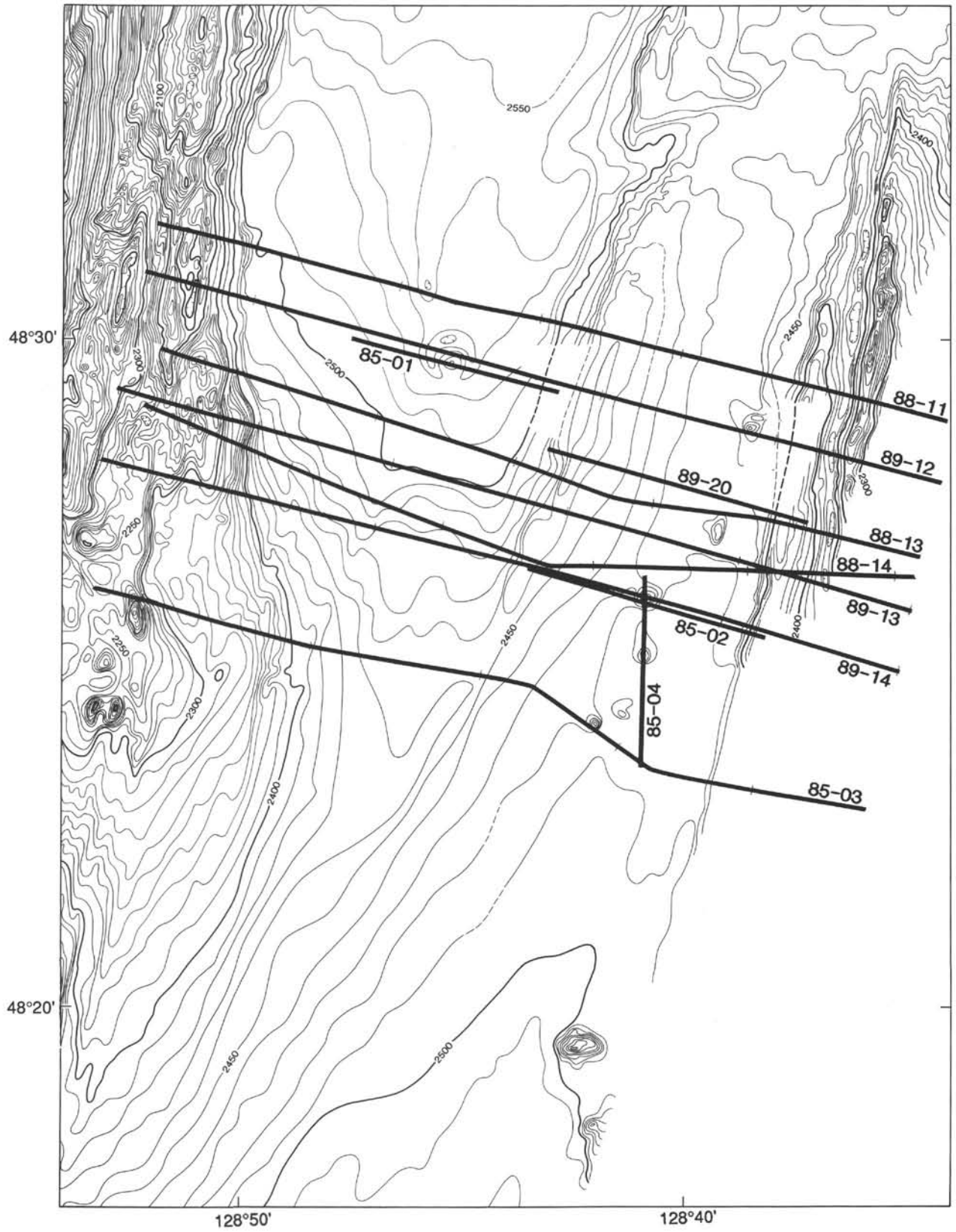


Figure 4. Bathymetry of the detailed study area discussed in this paper, contoured at 10-m intervals. Depths are derived from SeaBeam soundings and computed from traveltimes assuming a sound velocity of 1500 m/s. Data are derived from published maps of Currie et al. (1985) and have been navigationally adjusted according to identifiable features located during more recent surveys having global positioning system (GPS) control. Tracklines of seismic profiles shown in Figures 3 and 6 are indicated.

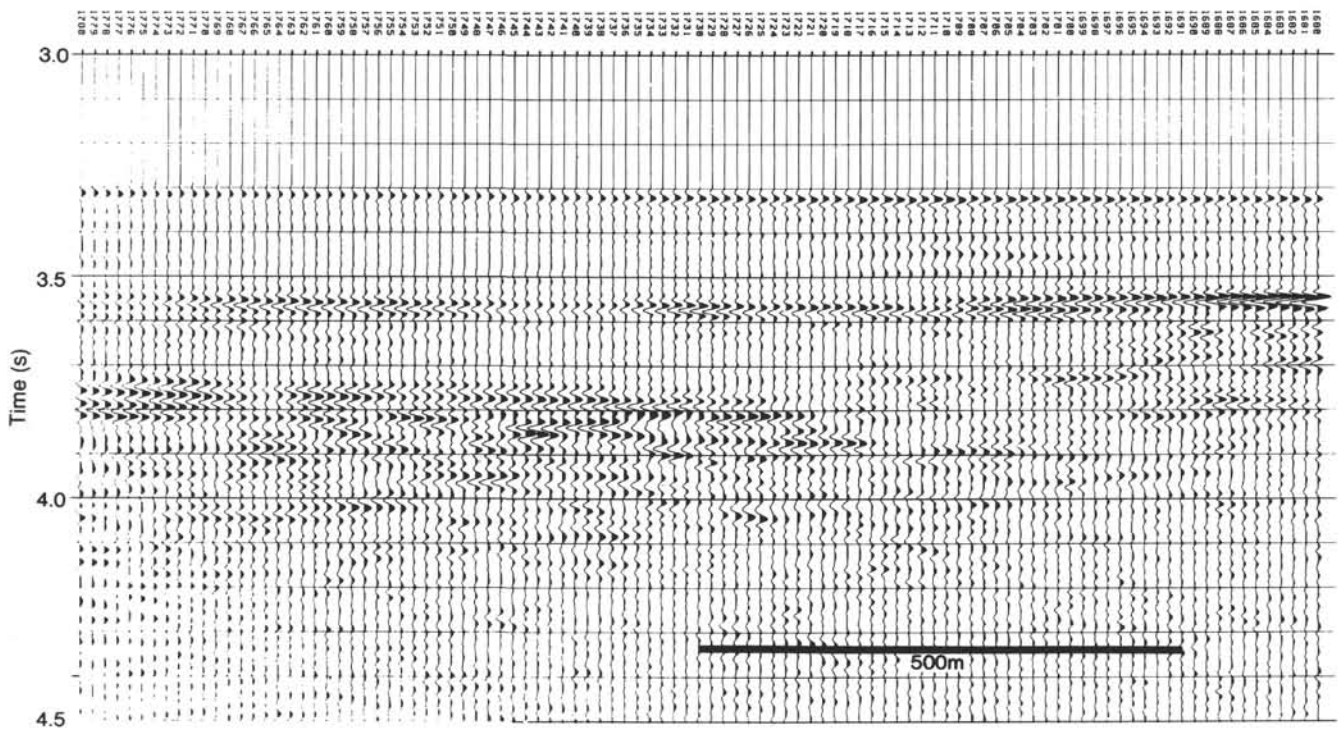


Figure 5. Trace-by-trace display of a portion of line 89-13 (near kilometer 8 east) where a continuous, high-amplitude reflector can be seen within the sediment section, and where the reflection character of acoustic basement is particularly reverberant (plot provided by K. Rohr).

Recent Local Intrusive Activity

One example of a bright reflector is associated with an unusual seafloor structure. It is situated near the center of the main part of the rift valley and is crossed by line 89-12 (Fig. 3; 2 km east of the axial reference line) and by line 85-01 (Fig. 6A). Above the reflector that lies 0.5 s below the seafloor, the seismic stratigraphy of the sediment section is disrupted to the point that the local sequence of reflectors cannot be traced through with confidence. The coherency of the stratigraphy beneath the bright reflector at 0.5 s is completely lost, and the structure deeper within the sediment section is not imaged. A 3.5-kHz echo-sounding profile collected with seismic line 85-10 shows the central part of the structure to be uplifted about 15 m above the surrounding undisturbed seafloor. This is surrounded by a moat that lies up to 25 m below the surrounding seafloor, which is in turn surrounded by a slightly elevated rim. The plan form of the feature can be seen in both the bathymetry (Fig. 4) and SeaMARC II acoustic imagery (Fig. 2C). It is roughly equidimensional, with an overall diameter of about 2 km. A higher resolution SeaMARC I image of the feature shows the surface morphology more clearly (Fig. 7). The disturbed area is seen to comprise three or four similar coalescing structures. The primary domed area is characterized by suborthogonal fractures, and the outer rim of the moat is riddled with closely spaced fault scarps that face inward toward the deepest part of the moat. Several small circular depressions can be seen nearby in the acoustic imagery.

The coincidence of the surface deformation and the bright reflection beneath strongly suggests that the deformation is the simple and direct consequence of the high-level intrusion that is imaged seismically. Similar structures occur in Escanaba Trough (Davis and Becker, 1992; Dellinger and Holmes, 1992), although they differ in detail. In many of those examples, the sediment is domed and uplifted by an amount considerably greater than that seen here (up to 150 m), and while intrasedimentary intrusions (bright reflectors) are common

there also, there is no direct correlation between the surface deformation and the disposition of the reflectors. In those cases, the deformation and uplift of the sediment section is inferred to be related primarily to larger volume intrusions near or below the bottom of the sediment section, not directly to the high-level intrusions that produce the intrasedimentary bright reflections.

Although the details of the intrusive structure seen in Middle Valley cannot be resolved, a limiting age can be established. For the same reasons discussed above, an upper limit for the age of the deformation seen at the seafloor is 10,000 yr. An additional constraint is provided by heat flow measurements across the feature (see discussion below) which suggest the age of intrusion to be younger still, probably less than a few thousand years.

The seismic line crossing the valley to the north of the structure (line 88-11) reveals more widespread and intense disruption of the deeper part of the sediment section, although the disruption there does not fully penetrate to the top of the sediment section. A history of volcanism spanning a significant part of the history of sedimentation in this part of Middle Valley is implied.

Other Local Structures

Most of measurements of the detailed heat flow study discussed below are concentrated in the eastern third of Middle Valley, over the series of uplifted but buried basement blocks between the eastern central-rift bounding fault (Fig. 3, 5 km east of the axial line) and the first normal-fault scarp that exposes basement (12 km east of the axial line).

Numerous small hills are present in this area. Two appear along seismic reflection profiles 89-12 and 89-14 (Fig. 3) and others appear in the bathymetry and side-scan imagery in Figures 2 and 4. The hills are circular, commonly several tens of meters high, and several hundred meters across. They are constructed of uplifted sediment and are cored by bright reflectors typically about 100 ms below their surfaces. Extensive, buried lava flows or sills are also seen in their

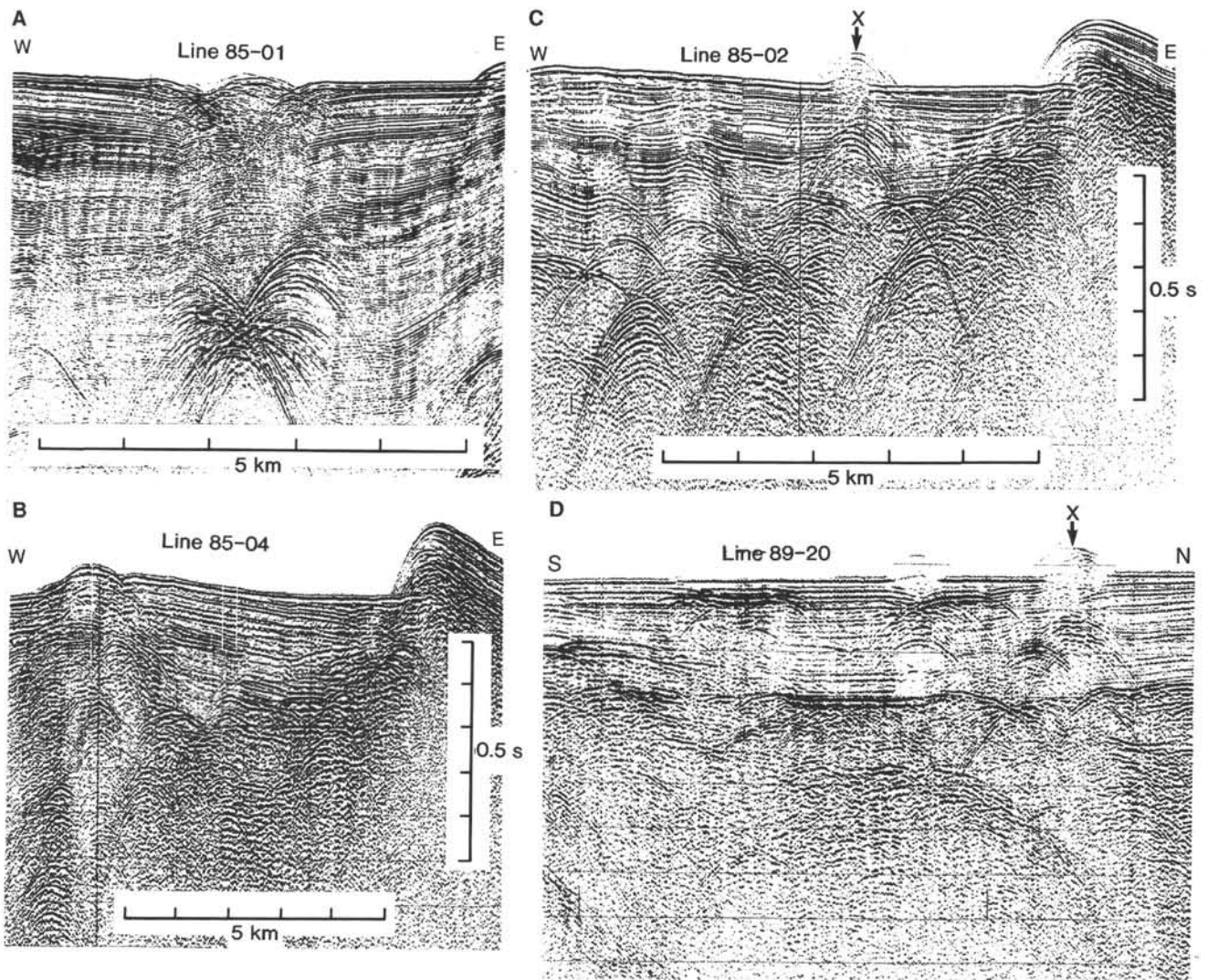


Figure 6. Single-channel seismic sections of several small-scale structures in Middle Valley. Line 85-01 (A) crosses a recent intrusion at the center of the rift valley. Lines 85-04 (B) and 85-02 (C) cross the structure referred to as "Bent Hill," where the sediment section has been uplifted above a laccolithic intrusion that lies roughly 100 ms beneath the seafloor. Arrows indicate points of intersection. Line 89-20 (D) crosses a buried basement edifice that underlies the "Dead Dog" vent field just east of the eastern bounding fault of the central rift. Depths scales are identical on all profiles. Locations of the profiles are given in Figure 4.

immediate vicinity. Detailed sections of one of the hills are shown in Figure 6B, 6C. Numerous detailed sampling and seafloor observational studies have been conducted at one of these structures where hydrothermal mineralization has been found (Davis, Goodfellow, et al., 1987; J. Franklin, W. Goodfellow, and J. Lydon, pers. comm., 1991; "Site 856" chapter, this volume). There are no heat flow anomalies directly associated with any of the hills; all appear to be thermally extinct. Their ages are not well constrained, but must fall between the time most of the sediment was deposited in this part of the valley (i.e., a few tens of thousands of years) because of the high level in the surrounding sediment at which the neighboring sills or flows are found (Fig. 6B), and a few thousand years, because of the lack of associated thermal anomalies. Although smaller and older relative to the crust on or in which they reside, these structures have many characteristics in common with the larger domes that occur in Escanaba Trough, and with the structure in the center of the Middle Valley rift described above. The genetic relationship between the hydrothermal mineralization and the structures is not understood.

THERMAL STRUCTURE OF THE VALLEY

Heat Flow Determinations

The thermal structure of southern Middle Valley is established by roughly 550 heat flow measurements. These were made typically along seismic reflection profiles using a Lister-type probe which has a multiple-thermistor array (of either 7 or 11 thermistors) and a heater wire supported within an 8-mm-diameter tube held in tension beside a 65-mm-diameter strength member (see Hyndman, Davis, and Wright, 1979, for a general description). Thermistors were spaced evenly down probes that varied from 2 to 4 m in length. A low-resolution acoustic link allowed the state of the instrument to be monitored at all times. Full resolution data (12 bits in 1984, 1985, and 1986 measurements, and 16 bits in 1989 measurements) were recorded internally. In the older instrument, a linearized response over a range of 12 K provided roughly 2-mK resolution. In the more recent version of the instrument, the digital resolution and the nonlinear response characteristics of the ther-

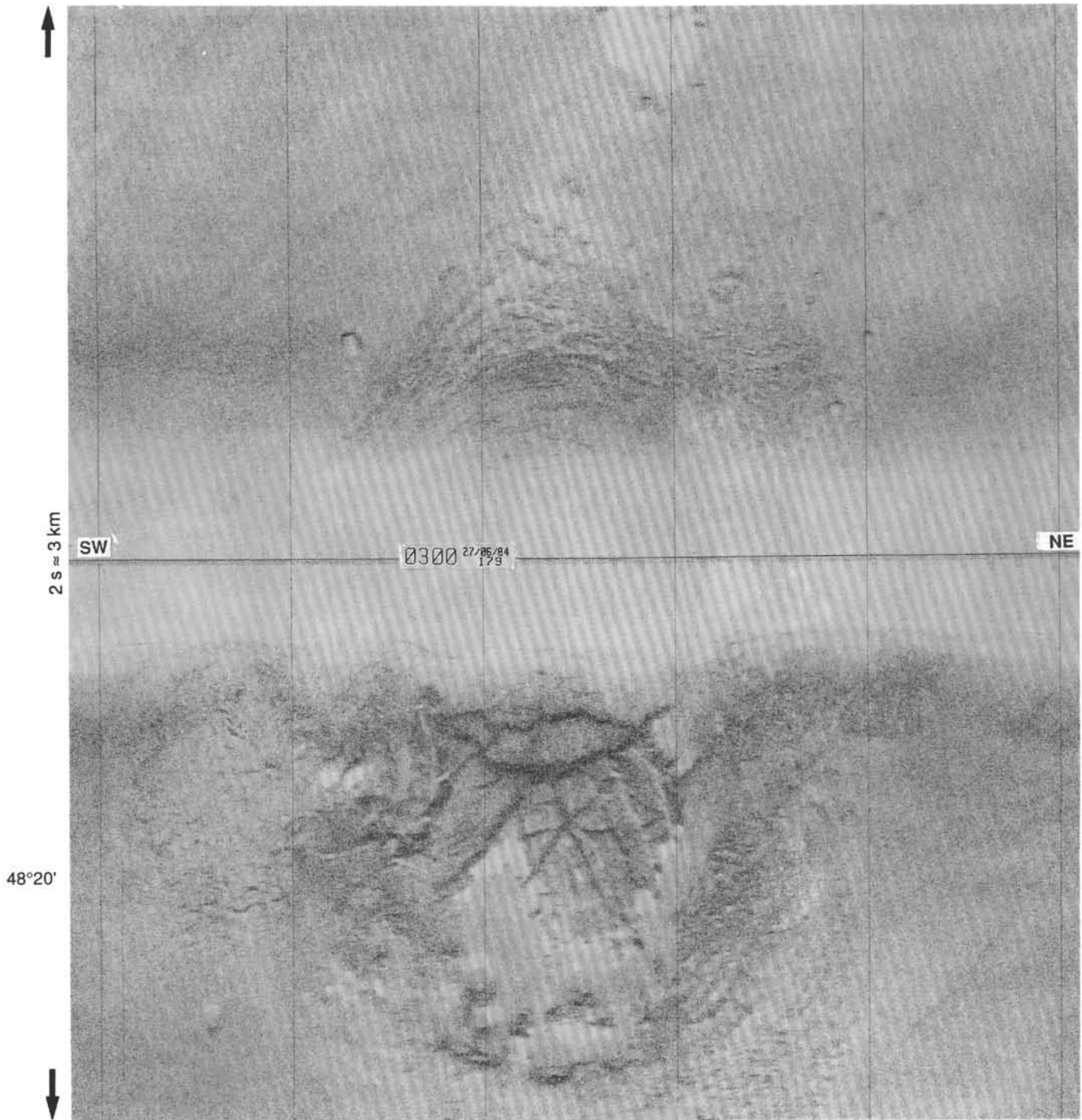


Figure 7. 30-kHz (SeaMARC I) slant-range side-scan acoustic image of the surface deformation above the intrusion in central Middle Valley that is crossed by seismic line 89-12 (Fig. 3) and line 85-01 (Fig. 6A).

mistors allowed relative temperatures of each of the probe sensors, a water temperature sensor, and an internal temperature sensor to be determined with a precision of roughly 0.5 mK at low temperatures (ca. 0°C), while maintaining a useful range of over 50 K. Tilt and absolute pressure were determined by the newer instrument. Tilt was used to assess the quality of questionable penetrations, and pressure to assist in the hindsight navigation of the probe as well as for automatic detection of penetrations by a heat-pulse-firing circuit. All channels, including low temperature-coefficient refer-

ence resistors and an internal temperature sensor, were sampled and logged every 10 s.

Typical penetrations included (1) a brief period during which a “zero-gradient” reference was obtained with the instrument held in the near-bottom water, (2) an undisturbed period of 7 min in the bottom while the sensor string equilibrated, and (3) an additional period of roughly 7 min while the decay of a calibrated heat pulse was monitored. From these data the thermal gradient and thermal conductivity were determined in the manner described in detail by Villinger

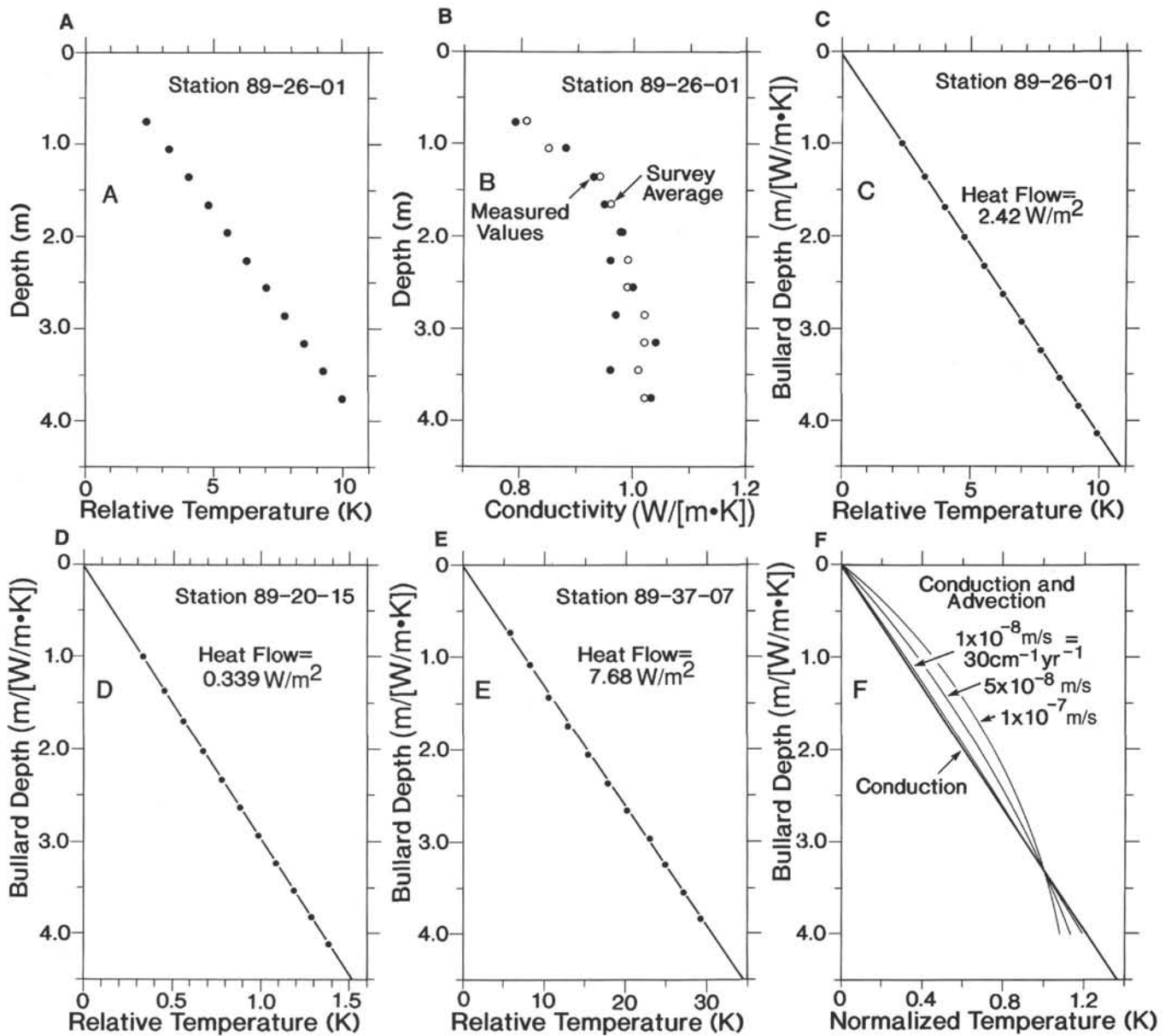


Figure 8. Plots of temperature vs. depth (A), thermal conductivity vs. depth (B), and temperature vs. integrated thermal resistance (Bullard depth) (C) for a typical heat flow measurement in Middle Valley. Also shown are Bullard plots of relatively low (D) and high (E) heat flow values to illustrate the linearity of the Bullard plots over the wide range of heat flow observed. Temperatures are plotted relative to the local bottom-water temperature (1.8°C) measured by a thermistor mounted on top of the instrument weight stand. A theoretical Bullard plot (F) is also shown to illustrate the limited sensitivity of the measurements to advective heat transport that would be caused by vertical pore fluid flow (following the model of Bredehoeft and Papadopoulos, 1965).

and Davis (1987). Data from several measurements are shown in Figure 8; the final heat flow values are computed as the slopes of temperature vs. vertically integrated thermal resistance. Thermal conductivity measurements were not made during many of the penetrations (see Table 1), either inadvertently because of premature probe disturbances, or deliberately as a trade-off between fewer complete measurements and more gradient measurements. For consistency, an assumed conductivity structure, derived from the average measured conductivity-depth structure determined from all measurements, was used to determine the heat flow at all penetrations. As can be seen in Figure 8B, there is a substantial variation in the conductivity with depth; this is the largest source of uncertainty in the heat flow determinations at most penetrations.

Uncertainties in the positions of the measurements vary considerably. Measurements made in 1989 were located by acoustic transponder net which was adjusted to match global positioning system (GPS) position determinations. Navigational inaccuracies are estimated to be about ± 50 m. All other measurement locations were determined by estimating the position of the probe with respect to the ship, the navigation for which was provided by GPS fixes or Ioran-C fixes adjusted to GPS or transit satellite coordinates. Wherever possible, the distance between the probe and the ship was determined by correlating images of structures recognized both on the ship's 3.5-kHz echo-sounding system and subsequently on the record of the probe's 3.5-kHz pinger. In these cases, penetrations are probably located with an uncertainty of about ± 100 m along the direction of travel during

the station. The azimuth from the ship to the probe was usually well determined as a result of the consistent orientation of the ship's track during a given heat flow station, and the cross-track uncertainty in position is estimated to be about ± 50 m. In the cases where no identifiable structures can be seen on the pinger and echo-sounding records, the along-track uncertainty is probably closer to ± 200 m. All results, including penetration locations, are included in Table 1.

Heat Flow Variations

In most areas of the valley heat flow variations are well defined by the measurements, which are spaced typically a few hundred meters apart, and this permits the heat flow to be contoured with reasonable confidence. The distribution of values is shown in this way in Figure 9A. Variations are large both regionally and locally; values range over more than two orders of magnitude, from about 0.15 to nearly 25 W/m^2 .

Along the axis of the valley, values generally tend to decrease toward the northern, most thickly sedimented part of the rift. Values decrease from roughly 0.6–0.8 W/m^2 near 48°25' N to about 0.160 W/m^2 in the deepest part of the valley within the survey area. This general inverse correlation between heat flow and sediment thickness (compare Fig. 9A, 9B) has been noted in previous measurements in the area (Davis and Lister, 1977a) and observed in ridge flank environments (e.g., Davis et al., 1989, in press; Fisher et al., 1990), and is thought simply to reflect the influence of a low-permeability, variable-thickness sediment layer blanketing a roughly isothermal, highly permeable basement. This is discussed further below.

Measurements near the shallow intrusion near the center of the rift are coarsely spaced, and the local variation in heat flow may not be well resolved. A small anomaly is present, however, with the maximum value over the structure (321 mW/m^2) being roughly 90 mW/m^2 higher than the local background values. Thus the intrusion must be sufficiently old for a weak thermal signal to have propagated the 500 m distance to the seafloor (i.e., greater than about 1000 yr). The lack of high values suggests that no hydrothermal discharge has been initiated by the intrusive event, and this indicates that the sediment deformation observed at this location has not significantly enhanced the permeability of the sediment section.

Consistently high values (greater than 1.0 W/m^2) occur in the westernmost part of the area, near where current rifting extends north from Endeavour Valley (Fig. 2A). As discussed earlier, the sediment surface in the area is domed, possibly as a result of recent intrusive activity which could be the cause for the elevated heat flow. The high heat flow also could be a result of the locally thinned sediment cover (see Figs. 3 and 9B and discussion below).

Over the buried basement bench east of the rift axis, numerous high-amplitude, highly localized heat flow anomalies occur. Most of these peak at values greater than 1 W/m^2 , and are typically several hundred meters to a kilometer in extent. High-temperature (ca. 270°C) fluid discharge at discrete vents, and hydrothermal mineralization are known to occur at two of these locations (J. Franklin, pers. comm., 1991; "Site 856" and "Site 858" chapters, this volume). These two examples are discussed below.

Measurements in the vicinity of the normal faults that bound the valley indicate that the faults or basement exposures along the faults serve as conduits for both fluid discharge and recharge. Two local high heat flow anomalies occur on the hanging wall blocks near the base of the fault scarps and indicate the presence of fluid seepage or venting. Although not well characterized by the measurements, these anomalies appear to be situated typically a few hundred meters away from the scarps themselves. Elsewhere, measurements indicate that fluids enter the crust along the scarps and pass into the footwall blocks (see discussion below).

Extrapolation of the Near-Surface Gradients

To better understand the thermal regime at depth requires extrapolation of the seafloor thermal-gradient measurements down through the sediment section, which in turn requires an estimate of the sediment thermal conductivity. Estimates of the average physical properties of the sediment section in Middle Valley have been derived from electrical resistivity measurements by Nobes et al. (1986). In this chapter, an estimate of the thermal conductivity as it varies with depth is derived from multichannel seismic reflection velocity data, using empirical relationships between velocity and porosity and between porosity and thermal conductivity.

A compilation of average velocities, calculated from the best-determined stacking velocities derived from semblance analyses along MCS lines 89-12, -13, and -14, is shown in Figure 10 (open circles). The data are scattered, in part because of the structural complexity present along the seismic lines, and the potential error of a velocity-depth relationship fitted through them is large. Simpler structure is found on the flank of the ridge along a multichannel line striking across Cascadia Basin directly to the east (K. Rohr, pers. comm., 1991). Velocities derived from the Cascadia Basin data are more tightly clustered (Fig. 10, solid circles), and probably contain less error. A linear regression through the Cascadia velocity vs. travelt ime points fits well, and suggests a relationship of $V_{average}$ (m/s) = 1552 + 510 · t , where t = two-way travelt ime in seconds below the seafloor. It should be noted that velocities determined in Middle Valley appear to be systematically higher than those in Cascadia Basin (Fig. 10), and thus a systematic error on the order of 5%–10% may be present in the physical properties estimated below.

Thermal conductivity of relatively high-porosity sediment is primarily a function of porosity, which can be estimated directly from velocity. Numerous empirical relationships exist relating velocity to porosity. Many are based on measurements made on core samples collected from the upper few meters of sediment sections (e.g., Hamilton, 1978) where the porosity is dependent primarily on lithology rather than the state of consolidation, or on deeper drill-core samples that may have undergone a high degree of drilling disturbance (e.g., Nobes et al., 1986). Data are commonly highly scattered and fits are ill constrained. A different approach was taken by Jarrard et al. (1989), who established a relationship between *in-situ* determinations of velocity and porosity with roughly 3500 velocity and porosity log measurements in a 750-m-thick section of terrigenous sediment penetrated at ODP Site 646 in the Labrador Sea. Their observations are represented by contours of data density (at unspecified intervals) in Figure 11.

At low porosities, the seismic velocity becomes sensitive to the rigidity of the matrix as well as the porosity. Han et al. (1986) found that the dominant factor controlling the matrix properties was the clay content. To account for the differences that may exist between the mineralogical constituents from one area to another, a simple correction can be applied to the relationship of Jarrard et al. (1989) to account for variations in the percentage of clay minerals. The uncorrected relationship of Jarrard et al. merges extremely well with the relationship of Han et al. for shales containing 50% clay (see Fig. 11). This is encouraging, as this clay content is very close to the average of values determined in the Labrador Sea section. A single third-order polynomial is fit through the two relationships in Figure 11 ($\phi = a_0 + a_1/v + a_2/v^2 + a_3/v^3$, where $a_0 = -1.180$, $a_1 = 8.607$, $a_2 = -17.894$, and $a_3 = 13.941$). At other values of clay content, corrections are applied to the relationship of Jarrard et al. in a way that forces the high-porosity curve to merge with the appropriate shale value at $\phi = 20\%$. This correction factor decreases linearly to zero at high porosity (75%), where the matrix compressibility should become unimportant. The clay mineral content of the sediment of Middle Valley is assumed

Table 1. Table of heat determinations in Middle Valley.

Cruise	Pen. ^a	Location Lat. (N), Long. (W)	Heat flow (mW/m ²)	Number of sensors
Station 1				
PGC84-4	1	48° 28.17', 128° 46.95'	404	5
PGC84-4	3	48° 27.87', 128° 47.84'	397	4
Station 2				
PGC84-4	1	48° 34.29', 128° 41.15'	371	7
PGC84-4	2	48° 34.25', 128° 41.34'	262	7
PGC84-4	3	48° 34.26', 128° 41.58'	267	7
PGC84-4	4	48° 34.22', 128° 41.68'	338	4
PGC84-4	5	48° 33.92', 128° 41.86'	388	4
PGC84-4	6	48° 33.73', 128° 42.04'	359	5
PGC84-4	8	48° 33.44', 128° 42.25'	474	4
PGC84-4	10	48° 33.00', 128° 42.36'	587	4
PGC84-4	11	48° 32.87', 128° 42.60'	494	5
PGC84-4	12	48° 32.72', 128° 42.87'	413	7
PGC84-4	14	48° 32.13', 128° 43.24'	335	7
PGC84-4	15	48° 31.78', 128° 43.43'	302	7
PGC84-4	16	48° 31.37', 128° 43.69'	278	7
PGC84-4	17	48° 31.03', 128° 44.00'	305	7
PGC84-4	18	48° 30.59', 128° 44.38'	306	6
PGC84-4	19	48° 30.44', 128° 44.58'	217	5
Station 3				
PGC84-4	1	48° 31.20', 128° 48.99'	165	5
PGC84-4	2	48° 31.41', 128° 48.23'	159	7
PGC84-4	3	48° 31.49', 128° 47.59'	161	7
PGC84-4	4	48° 31.39', 128° 46.99'	150	7
PGC84-4	5	48° 30.96', 128° 46.41'	169	5
PGC84-4	6	48° 30.53', 128° 46.17'	133	5
PGC84-4	8	48° 29.69', 128° 45.90'	230	5
PGC84-4	10	48° 29.55', 128° 45.83'	263	4
PGC84-4	11	48° 29.12', 128° 45.72'	268	7
PGC84-4	12	48° 28.80', 128° 45.58'	272	7
PGC84-4	13	48° 28.43', 128° 45.14'	309	7
PGC84-4	14	48° 28.14', 128° 44.85'	348	7
PGC84-4	16	48° 27.49', 128° 44.53'	424	7
PGC84-4	17	48° 27.04', 128° 44.34'	412	5
PGC84-4	18	48° 26.83', 128° 44.23'	1005	4
Station 4				
PGC84-4	1	48° 30.66', 128° 46.92'	151	5
PGC84-4	2	48° 30.63', 128° 46.82'	189	5
PGC84-4	3	48° 30.43', 128° 46.33'	120	7
PGC84-4	4	48° 30.32', 128° 46.01'	203	7
PGC84-4	5	48° 30.14', 128° 45.64'	299	6
PGC84-4	6	48° 30.03', 128° 45.39'	320	6
PGC84-4	7	48° 29.88', 128° 45.01'	246	7
PGC84-4	9	48° 29.57', 128° 44.26'	206	7
PGC84-4	10	48° 29.43', 128° 43.93'	341	5
PGC84-4	11	48° 29.28', 128° 43.64'	395	5
PGC84-4	12	48° 29.20', 128° 43.36'	390	7
PGC84-4	14	48° 28.93', 128° 42.88'	570	7
PGC84-4	15	48° 28.80', 128° 42.57'	744	7
Station 5				
PGC84-4	1	48° 27.25', 128° 43.20'	774	7
PGC84-4	2	48° 27.25', 128° 43.08'	1073	7
PGC84-4	3	48° 27.31', 128° 42.77'	2894	4
PGC84-4	4	48° 27.26', 128° 42.32'	1528	7
PGC84-4	5	48° 26.95', 128° 42.04'	1313	7
PGC84-4	6	48° 26.78', 128° 41.77'	729	7
PGC84-4	7	48° 26.60', 128° 41.57'	581	7
PGC84-4	8	48° 26.41', 128° 41.33'	605	7
PGC84-4	9	48° 26.30', 128° 41.18'	707	7
PGC84-4	10	48° 26.18', 128° 41.04'	1507	7
PGC84-4	11	48° 25.99', 128° 40.78'	3200	4
PGC84-4	12	48° 25.90', 128° 40.66'	2129	6
PGC84-4	13	48° 25.81', 128° 40.20'	883	7
PGC84-4	14	48° 25.78', 128° 40.00'	684	7
PGC84-4	15	48° 25.80', 128° 39.98'	556	7
PGC84-4	16	48° 25.80', 128° 39.76'	466	7
Station 6				
PGC84-4	1	48° 24.08', 128° 43.68'	841	5
PGC84-4	2	48° 24.10', 128° 43.57'	677	6
PGC84-4	3	48° 24.11', 128° 43.43'	995	7
PGC84-4	4	48° 24.14', 128° 43.17'	772	7

Table 1 (continued).

Cruise	Pen. ^a	Location Lat. (N), Long. (W)	Heat flow (mW/m ²)	Number of sensors
PGC84-4	5	48° 24.07', 128° 42.89'	659	7
PGC84-4	6	48° 24.04', 128° 42.54'	654	7
PGC84-4	7	48° 24.02', 128° 42.09'	683	7
PGC84-4	8	48° 23.97', 128° 41.76'	687	7
PGC84-4	9	48° 23.93', 128° 41.50'	616	7
PGC84-4	10	48° 23.71', 128° 41.24'	631	6
PGC84-4	11	48° 23.48', 128° 41.04'	788	7
PGC84-4	12	48° 23.38', 128° 40.74'	690	7
PGC84-4	13	48° 23.43', 128° 40.41'	589	7
PGC84-4	14	48° 23.44', 128° 40.04'	589	7
PGC84-4	15	48° 23.42', 128° 39.73'	648	7
PGC84-4	16	48° 23.37', 128° 39.32'	686	7
PGC84-4	17	48° 23.35', 128° 39.06'	548	7
PGC84-4	18	48° 23.25', 128° 38.55'	699	7
PGC84-4	19	48° 23.19', 128° 38.25'	787	7
PGC84-4	20	48° 23.14', 128° 37.96'	902	7
PGC84-4	21	48° 23.07', 128° 37.66'	534	7
PGC84-4	22	48° 23.04', 128° 37.29'	465	7
PGC84-4	23	48° 22.98', 128° 36.85'	355	7
PGC84-4	24	48° 23.01', 128° 36.34'	304	5
Station 7				
PGC84-4	1	48° 23.73', 128° 50.42'	1319	6
PGC84-4	2	48° 23.66', 128° 50.03'	1429	6
PGC84-4	3	48° 23.48', 128° 49.74'	1497	7
PGC84-4	4	48° 23.44', 128° 49.41'	952	7
PGC84-4	5	48° 23.34', 128° 48.94'	865	7
PGC84-4	6	48° 23.30', 128° 48.46'	763	7
PGC84-4	8	48° 23.14', 128° 47.43'	602	7
PGC84-4	9	48° 23.02', 128° 47.10'	598	7
PGC84-4	10	48° 23.10', 128° 46.80'	586	7
PGC84-4	11	48° 23.17', 128° 46.32'	539	7
PGC84-4	12	48° 23.24', 128° 46.00'	510	6
PGC84-4	13	48° 23.27', 128° 45.56'	487	7
PGC84-4	14	48° 23.34', 128° 45.09'	530	6
PGC84-4	15	48° 23.35', 128° 43.97'	914	7
PGC84-4	16	48° 23.34', 128° 43.28'	758	7
PGC84-4	17	48° 23.36', 128° 42.93'	666	7
PGC84-4	18	48° 23.44', 128° 42.66'	620	5
PGC84-4	19	48° 23.45', 128° 42.32'	553	5
Station 12				
PGC85-10	1	48° 26.30', 128° 45.49'	573	3
PGC85-10	2	48° 26.25', 128° 45.31'	559	7
PGC85-10	3	48° 26.21', 128° 45.23'	594	6
PGC85-10	4	48° 26.17', 128° 45.00'	641	3
PGC85-10	6	48° 26.14', 128° 44.24'	567	6
PGC85-10	7	48° 26.16', 128° 44.02'	661	7
PGC85-10	8	48° 26.14', 128° 43.44'	704	7
PGC85-10	9	48° 26.15', 128° 42.88'	812	7
PGC85-10	10	48° 26.10', 128° 42.25'	857	7
PGC85-10	11	48° 26.13', 128° 41.73'	653	7
PGC85-10	12	48° 26.14', 128° 41.51'	594	7
PGC85-10	13	48° 26.12', 128° 41.22'	637	7
PGC85-10	14	48° 26.10', 128° 40.88'	1665	5
PGC85-10	15	48° 26.09', 128° 40.61'	2298	4
PGC85-10	16	48° 26.09', 128° 40.25'	727	6
PGC85-10	17	48° 26.12', 128° 39.59'	419	7
PGC85-10	18	48° 26.13', 128° 39.03'	218	6
PGC85-10	21	48° 26.16', 128° 37.76'	290	7
Station 17				
PGC85-10	1	48° 17.42', 128° 41.60'	532	6
PGC85-10	3	48° 17.87', 128° 41.88'	1101	4
PGC85-10	5	48° 18.58', 128° 42.17'	387	7
PGC85-10	6	48° 18.99', 128° 42.47'	278	5
PGC85-10	7	48° 19.34', 128° 42.84'	325	6
PGC85-10	8	48° 19.74', 128° 43.09'	322	7
PGC85-10	9	48° 20.08', 128° 43.36'	395	6
PGC85-10	10	48° 20.33', 128° 43.50'	422	6
PGC85-10	11	48° 20.94', 128° 43.89'	502	4
PGC85-10	12	48° 21.69', 128° 44.32'	550	6
PGC85-10	13	48° 22.04', 128° 44.50'	788	7
PGC85-10	14	48° 22.33', 128° 44.63'	935	7
PGC85-10	15	48° 22.75', 128° 44.77'	673	7
PGC85-10	16	48° 23.09', 128° 44.90'	586	7
PGC85-10	18	48° 23.96', 128° 45.52'	587	7

Table 1 (continued).

Cruise	Pen. ^a	Location Lat. (N), Long. (W)	Heat flow (mW/m ²)	Number of sensors
Station 21				
PGC85-10	1	48° 17.15', 128° 46.59'	313	6
PGC85-10	2	48° 17.62', 128° 46.58'	290	6
PGC85-10	4	48° 18.66', 128° 46.61'	292	6
PGC85-10	5	48° 19.52', 128° 46.63'	322	6
PGC85-10	6	48° 19.82', 128° 46.63'	361	7
PGC85-10	7	48° 20.40', 128° 46.65'	353	6
PGC85-10	8	48° 20.61', 128° 46.60'	365	7
PGC85-10	9	48° 20.99', 128° 46.59'	354	7
PGC85-10	10	48° 21.11', 128° 46.75'	335	7
PGC85-10	11	48° 21.32', 128° 47.70'	303	7
PGC85-10	12	48° 21.50', 128° 48.82'	385	7
PGC85-10	13	48° 21.52', 128° 49.48'	469	7
PGC85-10	14	48° 21.51', 128° 49.68'	627	7
PGC85-10	15	48° 21.62', 128° 50.04'	807	7
PGC85-10	16	48° 21.63', 128° 50.54'	1022	7
PGC85-10	17	48° 21.75', 128° 51.00'	1289	7
PGC85-10	18	48° 22.01', 128° 51.50'	1150	7
PGC85-10	19	48° 22.26', 128° 51.95'	1095	7
PGC85-10	20	48° 22.69', 128° 52.94'	1158	7
PGC85-10	21	48° 23.01', 128° 53.98'	1076	7
Station 28				
PGC85-10	1	48° 21.15', 128° 46.41'	367	7
PGC85-10	2	48° 21.54', 128° 46.37'	341	7
PGC85-10	3	48° 23.51', 128° 46.41'	533	7
Station 29				
PGC85-10	1	48° 24.80', 128° 43.48'	858	7
PGC85-10	2	48° 24.89', 128° 43.93'	861	7
PGC85-10	3	48° 24.84', 128° 44.24'	740	7
PGC85-10	4	48° 24.85', 128° 44.76'	624	7
PGC85-10	5	48° 24.96', 128° 45.12'	679	7
PGC85-10	6	48° 25.10', 128° 45.87'	763	7
PGC85-10	7	48° 25.15', 128° 46.11'	698	6
PGC85-10	8	48° 25.17', 128° 46.47'	706	7
PGC85-10	9	48° 25.21', 128° 46.78'	743	7
PGC85-10	10	48° 25.31', 128° 47.10'	788	7
PGC85-10	11	48° 25.37', 128° 47.41'	881	6
PGC85-10	12	48° 25.48', 128° 47.84'	959	7
PGC85-10	13	48° 25.49', 128° 48.21'	1023	7
PGC85-10	14	48° 25.56', 128° 48.75'	1153	7
PGC85-10	15	48° 25.68', 128° 49.35'	1665	7
PGC85-10	16	48° 25.73', 128° 49.76'	1124	7
PGC85-10	17	48° 25.71', 128° 50.18'	888	7
PGC85-10	18	48° 25.75', 128° 50.68'	1018	7
PGC85-10	19	48° 25.72', 128° 50.84'	792	7
PGC85-10	20	48° 25.77', 128° 51.14'	912	7
PGC85-10	21	48° 25.81', 128° 51.38'	897	7
Station 36				
PGC85-10	1	48° 26.10', 128° 45.35'	765	4
PGC85-10	2	48° 26.30', 128° 45.75'	690	4
PGC85-10	3	48° 26.49', 128° 46.15'	546	6
PGC85-10	4	48° 26.64', 128° 46.59'	550	4
PGC85-10	5	48° 26.89', 128° 46.92'	502	7
PGC85-10	6	48° 27.05', 128° 47.30'	477	5
PGC85-10	7	48° 27.05', 128° 47.58'	481	4
PGC85-10	8	48° 27.28', 128° 48.16'	426	7
PGC85-10	9	48° 27.34', 128° 48.49'	477	4
PGC85-10	10	48° 27.38', 128° 49.03'	429	6
PGC85-10	11	48° 27.42', 128° 49.42'	540	7
PGC85-10	12	48° 27.54', 128° 49.83'	840	6
PGC85-10	13	48° 27.69', 128° 50.36'	1246	7
PGC85-10	14	48° 27.84', 128° 50.81'	1171	4
PGC85-10	15	48° 28.10', 128° 51.26'	1531	7
Station 41				
PGC85-10	1	48° 27.97', 128° 34.31'	416	6
PGC85-10	2	48° 28.02', 128° 34.66'	421	6
PGC85-10	3	48° 28.10', 128° 34.99'	481	6
PGC85-10	4	48° 28.15', 128° 35.28'	461	6
PGC85-10	5	48° 28.25', 128° 35.59'	444	6
PGC85-10	6	48° 28.36', 128° 35.75'	518	6
PGC85-10	7	48° 28.39', 128° 35.94'	221	5
PGC85-10	8	48° 28.47', 128° 36.58'	619	6
PGC85-10	9	48° 28.47', 128° 36.99'	358	6

Table 1 (continued).

Cruise	Pen. ^a	Location Lat. (N), Long. (W)	Heat flow (mW/m ²)	Number of sensors
PGC85-10	10	48° 28.59', 128° 37.25'	368	6
PGC85-10	11	48° 28.64', 128° 37.46'	363	6
PGC85-10	12	48° 28.66', 128° 37.66'	639	6
PGC85-10	13	48° 28.69', 128° 38.00'	526	6
PGC85-10	14	48° 28.71', 128° 38.56'	549	6
PGC85-10	15	48° 28.82', 128° 39.05'	411	6
Station 45				
PGC85-10	1	48° 27.06', 128° 36.51'	924	7
PGC85-10	2	48° 27.29', 128° 36.61'	1090	7
PGC85-10	3	48° 27.56', 128° 37.09'	425	7
PGC85-10	4	48° 27.38', 128° 37.45'	355	6
PGC85-10	5	48° 27.19', 128° 37.62'	387	7
PGC85-10	6	48° 27.12', 128° 37.76'	325	6
PGC85-10	7	48° 26.99', 128° 37.89'	250	7
PGC85-10	8	48° 26.95', 128° 38.04'	829	6
PGC85-10	10	48° 26.85', 128° 38.35'	631	6
PGC85-10	11	48° 26.89', 128° 38.51'	376	7
PGC85-10	12	48° 26.93', 128° 38.66'	470	6
PGC85-10	13	48° 26.92', 128° 38.80'	440	6
PGC85-10	14	48° 26.93', 128° 38.94'	418	6
PGC85-10	15	48° 26.92', 128° 39.11'	493	7
PGC85-10	17	48° 27.01', 128° 39.33'	396	7
Station 47				
PGC85-10	1	48° 25.89', 128° 44.02'	697	7
PGC85-10	2	48° 26.09', 128° 43.83'	698	7
PGC85-10	3	48° 26.40', 128° 43.62'	699	7
PGC85-10	4	48° 26.79', 128° 43.58'	680	7
PGC85-10	5	48° 27.15', 128° 43.45'	777	7
PGC85-10	6	48° 27.45', 128° 42.98'	1760	7
PGC85-10	7	48° 27.62', 128° 42.77'	1233	7
PGC85-10	8	48° 27.86', 128° 42.59'	1488	7
PGC85-10	9	48° 27.99', 128° 42.51'	1496	7
PGC85-10	10	48° 28.05', 128° 42.16'	963	7
PGC85-10	11	48° 28.29', 128° 41.96'	937	7
PGC85-10	12	48° 28.59', 128° 41.80'	1062	7
PGC85-10	13	48° 28.79', 128° 41.67'	1044	7
PGC85-10	14	48° 28.99', 128° 41.56'	1088	7
PGC85-10	15	48° 29.19', 128° 41.52'	896	7
PGC85-10	16	48° 29.62', 128° 41.27'	742	7
PGC85-10	17	48° 29.83', 128° 41.18'	637	7
PGC85-10	18	48° 30.12', 128° 41.10'	636	7
PGC85-10	19	48° 30.29', 128° 41.08'	519	7
PGC85-10	20	48° 30.60', 128° 40.90'	418	7
Station 50				
PGC85-10	1	48° 27.12', 128° 39.10'	453	6
PGC85-10	2	48° 27.12', 128° 39.20'	453	6
PGC85-10	3	48° 27.12', 128° 39.31'	362	7
PGC85-10	6	48° 27.08', 128° 39.65'	399	6
PGC85-10	7	48° 27.11', 128° 39.79'	386	7
PGC85-10	8	48° 27.17', 128° 40.03'	176	6
PGC85-10	9	48° 27.17', 128° 40.23'	153	6
PGC85-10	10	48° 27.21', 128° 40.59'	411	7
PGC85-10	11	48° 27.19', 128° 40.94'	426	7
PGC85-10	12	48° 27.15', 128° 41.21'	466	7
PGC85-10	13	48° 27.12', 128° 41.51'	524	7
PGC85-10	15	48° 27.27', 128° 41.89'	729	7
PGC85-10	16	48° 27.30', 128° 42.03'	994	7
PGC85-10	17	48° 27.40', 128° 42.23'	1663	7
PGC85-10	18	48° 27.44', 128° 42.42'	2653	5
PGC85-10	20	48° 27.56', 128° 42.57'	4439	3
PGC85-10	21	48° 27.73', 128° 42.67'	1898	7
PGC85-10	22	48° 27.75', 128° 42.75'	1099	7
PGC85-10	23	48° 27.77', 128° 42.93'	904	7
PGC85-10	24	48° 27.86', 128° 42.99'	832	5
PGC85-10	25	48° 27.99', 128° 42.89'	800	7
PGC85-10	26	48° 28.13', 128° 42.66'	862	7
PGC85-10	27	48° 28.22', 128° 42.49'	923	7
PGC85-10	28	48° 28.28', 128° 42.39'	1049	7
PGC85-10	29	48° 28.38', 128° 42.28'	1181	7
PGC85-10	30	48° 28.49', 128° 42.16'	1052	6
PGC85-10	31	48° 28.58', 128° 41.86'	851	7
PGC85-10	32	48° 28.63', 128° 41.66'	791	7
PGC85-10	33	48° 28.64', 128° 41.14'	609	7
PGC85-10	34	48° 28.68', 128° 40.77'	421	6

Table 1 (continued).

Cruise	Pen. ^a	Location		Heat flow (mW/m ²)	Number of sensors
		Lat. (N), Long. (W)			
PGC85-10	35	48° 28.71', 128° 40.44'		427	7
PGC85-10	36	48° 28.83', 128° 40.05'		390	7
Station 58					
PGC85-10	1	48° 28.11', 128° 43.95'		618	4
PGC85-10	2	48° 28.05', 128° 43.80'		606	3
PGC85-10	3	48° 27.95', 128° 43.56'		679	4
PGC85-10	4	48° 27.99', 128° 43.65'		872	7
PGC85-10	6	48° 27.67', 128° 43.23'		918	5
PGC85-10	7	48° 27.56', 128° 43.07'		1511	7
PGC85-10	9	48° 27.43', 128° 42.65'	24559	6	6
PGC85-10	10	48° 27.35', 128° 42.54'		3022	7
PGC85-10	11	48° 27.31', 128° 42.47'		1926	7
PGC85-10	12	48° 27.31', 128° 42.44'		1742	7
PGC85-10	13	48° 27.31', 128° 42.37'		1813	7
PGC85-10	14	48° 27.39', 128° 42.36'		2029	7
PGC85-10	15	48° 27.43', 128° 42.39'		2031	7
PGC85-10	16	48° 27.56', 128° 42.38'		1815	7
PGC85-10	17	48° 27.65', 128° 42.46'		1644	6
PGC85-10	18	48° 27.80', 128° 42.49'		1498	7
PGC85-10	19	48° 27.89', 128° 42.50'		1317	7
PGC85-10	20	48° 28.03', 128° 42.52'		1236	7
PGC85-10	21	48° 28.17', 128° 42.57'		1076	7
Station 61					
PGC85-10	1	48° 28.91', 128° 40.60'		418	7
PGC85-10	4	48° 28.56', 128° 40.44'		413	7
PGC85-10	5	48° 28.38', 128° 40.58'		406	7
PGC85-10	6	48° 28.19', 128° 40.64'		409	7
PGC85-10	7	48° 28.05', 128° 40.71'		412	7
PGC85-10	8	48° 27.92', 128° 40.81'		418	7
PGC85-10	9	48° 27.67', 128° 40.90'		420	7
PGC85-10	10	48° 27.43', 128° 41.01'		418	7
PGC85-10	11	48° 27.15', 128° 40.96'		433	7
PGC85-10	12	48° 26.90', 128° 40.98'		424	7
PGC85-10	13	48° 26.77', 128° 40.98'		362	7
PGC85-10	14	48° 26.64', 128° 40.97'		187	7
PGC85-10	15	48° 26.56', 128° 40.96'		509	7
PGC85-10	16	48° 26.51', 128° 40.97'		539	7
PGC85-10	17	48° 26.45', 128° 40.94'		584	7
PGC85-10	18	48° 26.35', 128° 40.90'		684	7
PGC85-10	20	48° 26.24', 128° 40.88'		632	7
PGC85-10	21	48° 26.20', 128° 40.90'		965	7
PGC85-10	22	48° 26.17', 128° 40.91'		764	5
PGC85-10	25	48° 25.81', 128° 40.93'		4907	7
PGC85-10	26	48° 25.68', 128° 41.00'		3646	7
PGC85-10	27	48° 25.53', 128° 41.01'		1484	7
PGC85-10	28	48° 25.30', 128° 40.97'		842	7
PGC85-10	29	48° 25.06', 128° 40.95'		600	7
PGC85-10	30	48° 24.61', 128° 40.93'		529	7
PGC85-10	31	48° 24.44', 128° 40.92'		307	7
PGC85-10	32	48° 24.13', 128° 40.93'		484	7
PGC85-10	33	48° 24.00', 128° 40.86'		298	6
PGC85-10	34	48° 23.87', 128° 40.81'		311	7
PGC85-10	35	48° 23.64', 128° 40.86'		270	7
PGC85-10	36	48° 23.45', 128° 40.79'		598	7
PGC85-10	37	48° 23.34', 128° 40.82'		781	7
PGC85-10	38	48° 23.19', 128° 40.83'		1314	7
PGC85-10	39	48° 23.01', 128° 40.95'		1405	7
PGC85-10	40	48° 22.88', 128° 40.98'		851	7
PGC85-10	41	48° 22.60', 128° 41.01'		606	7
Station 1					
PGC86-2	1	48° 24.96', 128° 42.95'		901	6
PGC86-2	2	48° 25.07', 128° 42.73'		757	7
PGC86-2	3	48° 25.23', 128° 42.41'		658	7
PGC86-2	4	48° 25.56', 128° 41.99'		641	6
PGC86-2	5	48° 25.75', 128° 41.57'		663	6
PGC86-2	6	48° 25.98', 128° 41.28'		885	7
PGC86-2	7	48° 26.18', 128° 41.06'		1062	7
PGC86-2	8	48° 26.39', 128° 40.74'		368	5
PGC86-2	10	48° 26.88', 128° 40.06'		393	6
PGC86-2	11	48° 27.28', 128° 39.32'		323	7
Station 5					
PGC86-2	1	48° 26.49', 128° 40.30'		469	7
PGC86-2	2	48° 26.48', 128° 40.26'		460	6

Table 1 (continued).

Cruise	Pen. ^a	Location		Heat flow (mW/m ²)	Number of sensors
		Lat. (N), Long. (W)			
PGC86-2	4	48° 26.70', 128° 39.88'		433	6
PGC86-2	5	48° 26.75', 128° 39.62'		404	6
PGC86-2	6	48° 26.71', 128° 39.44'		391	6
PGC86-2	7	48° 26.56', 128° 39.47'		407	6
PGC86-2	8	48° 26.32', 128° 39.55'		409	6
PGC86-2	9	48° 25.95', 128° 39.71'		432	7
PGC86-2	10	48° 25.80', 128° 39.68'		462	6
PGC86-2	11	48° 25.71', 128° 39.58'		276	7
PGC86-2	12	48° 25.57', 128° 39.59'		505	7
PGC86-2	13	48° 25.39', 128° 39.73'		491	6
PGC86-2	14	48° 25.13', 128° 39.93'		485	6
PGC86-2	15	48° 24.81', 128° 40.13'		454	7
PGC86-2	16	48° 24.48', 128° 40.26'		248	4
PGC86-2	17	48° 24.19', 128° 39.88'		451	6
PGC86-2	18	48° 24.20', 128° 39.58'		321	4
PGC86-2	19	48° 24.21', 128° 39.47'		526	7
PGC86-2	20	48° 24.26', 128° 38.82'		414	6
PGC86-2	21	48° 24.21', 128° 38.61'		433	7
PGC86-2	22	48° 24.06', 128° 38.54'		486	6
PGC86-2	23	48° 23.94', 128° 38.24'		583	7
Station 6					
PGC86-2	1	48° 29.39', 128° 37.77'		1239	6
PGC86-2	2	48° 29.30', 128° 37.87'		1207	7
PGC86-2	3	48° 29.20', 128° 38.02'		1262	7
PGC86-2	4	48° 29.11', 128° 38.20'		507	7
PGC86-2	5	48° 29.05', 128° 38.29'		508	6
PGC86-2	6	48° 28.97', 128° 38.32'		494	7
PGC86-2	7	48° 28.88', 128° 38.33'		478	7
PGC86-2	8	48° 28.69', 128° 38.34'		449	7
PGC86-2	9	48° 28.48', 128° 38.30'		535	7
PGC86-2	10	48° 28.29', 128° 38.24'		493	7
PGC86-2	11	48° 28.12', 128° 38.22'		552	7
PGC86-2	12	48° 27.98', 128° 38.18'		685	7
PGC86-2	13	48° 27.85', 128° 38.08'		962	3
PGC86-2	14	48° 27.72', 128° 38.25'		6555	7
PGC86-2	15	48° 27.48', 128° 38.44'		1294	6
PGC86-2	16	48° 27.18', 128° 38.35'		542	6
PGC86-2	17	48° 27.03', 128° 38.38'		503	6
PGC86-2	18	48° 26.82', 128° 38.44'		480	6
PGC86-2	19	48° 26.59', 128° 38.52'		479	6
PGC86-2	20	48° 26.45', 128° 38.55'		504	6
PGC86-2	21	48° 26.31', 128° 38.65'		475	6
PGC86-2	22	48° 26.23', 128° 38.74'		467	6
PGC86-2	23	48° 26.13', 128° 38.77'		480	6
PGC86-2	24	48° 26.00', 128° 38.85'		469	6
PGC86-2	25	48° 25.88', 128° 38.90'		469	6
PGC86-2	26	48° 25.69', 128° 38.95'		565	7
PGC86-2	27	48° 25.58', 128° 39.01'		644	6
PGC86-2	28	48° 25.43', 128° 39.09'		742	6
PGC86-2	29	48° 25.28', 128° 39.16'		712	6
PGC86-2	30	48° 25.09', 128° 39.18'		661	6
PGC86-2	31	48° 24.98', 128° 39.20'		605	4
PGC86-2	32	48° 24.82', 128° 39.25'		518	6
PGC86-2	33	48° 24.61', 128° 39.36'		566	4
PGC86-2	34	48° 24.46', 128° 39.40'		298	7
PGC86-2	35	48° 24.35', 128° 39.42'		496	6
Station 9					
PGC86-2	1	48° 25.85', 128° 41.48'		810	7
PGC86-2	2	48° 25.85', 128° 41.39'		907	7
PGC86-2	3	48° 25.85', 128° 41.32'		1134	7
PGC86-2	4	48° 25.84', 128° 41.19'		1648	7
PGC86-2	5	48° 25.82', 128° 41.01'		3092	7
PGC86-2	6	48° 25.82', 128° 40.79'		4714	7
PGC86-2	7	48° 25.82', 128° 40.53'		1872	7
PGC86-2	8	48° 25.84', 128° 40.28'		1072	7
PGC86-2	9	48° 25.61', 128° 39.85'		551	7
PGC86-2	10	48° 25.58', 128° 39.71'		502	7
PGC86-2	11	48° 25.41', 128° 39.23'		420	6
PGC86-2	12	48° 25.34', 128° 38.91'		305	5
Station 10					
PGC86-2	1	48° 25.01', 128° 35.61'		401	7
PGC86-2	2	48° 24.96', 128° 35.76'		407	7
PGC86-2	3	48° 24.93', 128° 35.92'		429	7
PGC86-2	4	48° 24.94', 128° 36.18'		460	7

Table 1 (continued).

Cruise	Pen. ^a	Location Lat. (N), Long. (W)	Heat flow (mW/m ²)	Number of sensors
PGC86-2	5	48° 24.94', 128° 36.41'	463	7
PGC86-2	6	48° 24.96', 128° 36.63'	416	7
PGC86-2	7	48° 25.02', 128° 36.87'	432	6
PGC86-2	8	48° 25.07', 128° 37.15'	589	7
PGC86-2	9	48° 25.09', 128° 37.46'	458	7
PGC86-2	10	48° 25.13', 128° 37.73'	506	6
PGC86-2	11	48° 25.16', 128° 37.92'	461	6
PGC86-2	12	48° 25.16', 128° 38.04'	451	7
PGC86-2	13	48° 25.17', 128° 38.12'	450	7
PGC86-2	14	48° 25.20', 128° 38.34'	411	7
PGC86-2	15	48° 25.21', 128° 38.49'	354	7
PGC86-2	16	48° 25.24', 128° 38.65'	365	6
PGC86-2	17	48° 25.24', 128° 38.79'	276	7
PGC86-2	18	48° 25.30', 128° 38.96'	656	7
PGC86-2	19	48° 25.28', 128° 39.17'	355	7
PGC86-2	20	48° 25.31', 128° 39.18'	558	6
PGC86-2	21	48° 25.30', 128° 39.50'	513	6
PGC86-2	22	48° 25.29', 128° 39.81'	484	6
PGC86-2	23	48° 25.30', 128° 39.94'	471	7
PGC86-2	24	48° 25.25', 128° 40.10'	520	7
PGC86-2	25	48° 25.21', 128° 40.32'	585	7
PGC86-2	26	48° 25.24', 128° 40.58'	309	6
PGC86-2	27	48° 25.33', 128° 40.72'	926	6
PGC86-2	28	48° 25.46', 128° 40.82'	1285	6
PGC86-2	29	48° 25.56', 128° 40.86'	1677	7
PGC86-2	30	48° 25.63', 128° 40.87'	1877	7
PGC86-2	31	48° 25.75', 128° 40.90'	3484	7
PGC86-2	32	48° 25.89', 128° 40.90'	4183	6
PGC86-2	34	48° 26.05', 128° 40.88'	979	7
PGC86-2	36	48° 26.20', 128° 41.12'	845	7
PGC86-2	37	48° 26.22', 128° 41.30'	652	7
PGC86-2	38	48° 26.28', 128° 41.53'	588	7
PGC86-2	39	48° 26.32', 128° 41.82'	584	7
PGC86-2	40	48° 26.38', 128° 42.00'	629	7
PGC86-2	41	48° 26.42', 128° 42.21'	699	7
PGC86-2	42	48° 26.44', 128° 42.38'	819	7
PGC86-2	43	48° 26.49', 128° 42.60'	1037	7
PGC86-2	44	48° 26.54', 128° 42.69'	999	7
PGC86-2	45	48° 26.65', 128° 42.88'	934	7
PGC86-2	46	48° 26.80', 128° 42.85'	882	7
PGC86-2	47	48° 26.91', 128° 42.82'	1001	7
PGC86-2	48	48° 27.08', 128° 42.77'	1113	7
PGC86-2	49	48° 27.18', 128° 42.73'	1716	7
PGC86-2	52	48° 27.51', 128° 42.51'	5393	7
PGC86-2	53	48° 27.64', 128° 42.42'	1866	7
PGC86-2	54	48° 27.77', 128° 42.33'	1292	7
PGC86-2	55	48° 28.01', 128° 42.31'	1477	7
PGC86-2	56	48° 28.22', 128° 42.18'	1708	7
PGC86-2	57	48° 28.40', 128° 42.12'	1293	7
PGC86-2	58	48° 28.62', 128° 42.02'	1088	7
Station 12				
PGC86-2	1	48° 28.22', 128° 39.63'	160	6
PGC86-2	2	48° 28.11', 128° 39.52'	371	7
PGC86-2	3	48° 28.02', 128° 39.39'	379	7
PGC86-2	4	48° 27.84', 128° 39.14'	443	7
PGC86-2	5	48° 27.81', 128° 38.95'	519	6
PGC86-2	6	48° 27.77', 128° 38.79'	697	6
PGC86-2	7	48° 27.78', 128° 38.41'	1127	6
PGC86-2	8	48° 27.75', 128° 38.26'	2489	7
PGC86-2	9	48° 27.75', 128° 38.10'	2421	7
PGC86-2	11	48° 27.63', 128° 37.58'	402	7
PGC86-2	12	48° 27.59', 128° 37.47'	371	7
PGC86-2	13	48° 27.57', 128° 37.35'	421	6
PGC86-2	14	48° 27.46', 128° 37.24'	472	7
PGC86-2	15	48° 27.37', 128° 36.97'	653	7
PGC86-2	16	48° 27.30', 128° 36.71'	1444	7
PGC86-2	17	48° 27.30', 128° 36.60'	1460	7
PGC86-2	18	48° 27.22', 128° 36.27'	541	7
PGC86-2	19	48° 27.14', 128° 35.92'	433	7
PGC86-2	20	48° 26.98', 128° 35.68'	417	7
PGC86-2	21	48° 26.84', 128° 35.51'	460	7
PGC86-2	22	48° 26.69', 128° 35.34'	433	6
Station 20				
PGC89-4	1	48° 27.52', 128° 37.99'	536	11
PGC89-4	2	48° 27.60', 128° 37.95'	617	11

Table 1 (continued).

Cruise	Pen. ^a	Location Lat. (N), Long. (W)	Heat flow (mW/m ²)	Number of sensors
PGC89-4	3	48° 27.77', 128° 37.94'	1162	11
PGC89-4	4	48° 27.70', 128° 38.00'	817	11
PGC89-4	5	48° 27.70', 128° 38.16'	860	11
PGC89-4	6	48° 27.65', 128° 38.21'	706	11
PGC89-4	7	48° 27.65', 128° 38.31'	806	11
PGC89-4	8	48° 27.60', 128° 38.60'	650	11
PGC89-4	9	48° 27.50', 128° 39.00'	476	11
PGC89-4	10	48° 27.50', 128° 39.44'	347	11
PGC89-4	11	48° 27.48', 128° 39.55'	323	11
PGC89-4	12	48° 27.49', 128° 39.74'	282	11
PGC89-4	13	48° 27.48', 128° 39.90'	295	11
PGC89-4	14	48° 27.49', 128° 40.13'	323	11
PGC89-4	15	48° 27.49', 128° 40.48'	338	11
PGC89-4	16	48° 27.54', 128° 40.98'	373	11
PGC89-4	17	48° 27.56', 128° 41.39'	405	11
PGC89-4	18	48° 27.56', 128° 41.77'	496	11
PGC89-4	19	48° 27.60', 128° 42.14'	1247	11
PGC89-4	20	48° 27.58', 128° 42.59'	10113	6
Station 26				
PGC89-4	1	48° 27.37', 128° 42.40'	2440	11
PGC89-4	2	48° 27.36', 128° 42.47'	6280	11
PGC89-4	3	48° 27.38', 128° 42.57'	13479	11
PGC89-4	4	48° 27.36', 128° 42.62'	10039	11
PGC89-4	5	48° 27.39', 128° 42.67'	7932	11
PGC89-4	6	48° 27.36', 128° 42.73'	2282	11
PGC89-4	7	48° 27.36', 128° 42.86'	1228	11
PGC89-4	8	48° 27.35', 128° 42.90'	1209	11
PGC89-4	9	48° 27.32', 128° 43.01'	1318	11
PGC89-4	10	48° 27.46', 128° 43.02'	1033	11
PGC89-4	11	48° 27.49', 128° 42.92'	1155	11
PGC89-4	12	48° 27.55', 128° 42.87'	1306	11
PGC89-4	13	48° 27.53', 128° 42.77'	1538	11
Station 37				
PGC89-4	1	48° 27.52', 128° 42.45'	6788	11
PGC89-4	2	48° 27.51', 128° 42.36'	2142	11
PGC89-4	3	48° 27.49', 128° 42.30'	1643	11
PGC89-4	4	48° 27.58', 128° 42.20'	1029	11
PGC89-4	5	48° 27.59', 128° 42.29'	1300	11
PGC89-4	6	48° 27.57', 128° 42.45'	4818	11
PGC89-4	7	48° 27.55', 128° 42.57'	7599	11
PGC89-4	8	48° 27.57', 128° 42.64'	4106	11
PGC89-4	9	48° 27.55', 128° 42.80'	1505	11
PGC89-4	10	48° 27.48', 128° 42.88'	1240	11
PGC89-4	11	48° 27.38', 128° 42.78'	1484	11
PGC89-4	12	48° 27.35', 128° 42.74'	1916	11
PGC89-4	13	48° 27.40', 128° 42.62'	4434	5
PGC89-4	14	48° 27.39', 128° 42.58'	15963	5
PGC89-4	15	48° 27.37', 128° 42.41'	2371	11
PGC89-4	16	48° 27.39', 128° 42.29'	1615	11

Notes: The length of the probe used from 1984 to 1986 was 2 m and included 7 temperature sensors. Measurements in 1989 were made with a 4-m-long probe with 11 sensors. All heat flow values that were calculated on the basis of the linear fit of thermal resistance vs. temperature have errors typically smaller than 2%. A greater error is associated with not knowing the conductivity at each penetration.

^aPenetration number.

to be the same as the average of values determined in Cascadia Basin at Deep Sea Drilling Project (DSDP) Site 174, roughly 45% (Zemmels and Cook, 1973). This is close to the average for the Labrador Sea section, and the correction applied to the relationship of Jarrard et al. is very small. Using the adjusted Jarrard/Han relationship between porosity and velocity with the interval-velocity depth profile shown in Figure 12A results in the porosity-depth profile shown in Figure 12B.

With this estimate for the porosity of the section, and an estimate of the average mineralogy, the thermal conductivity of the sediment can be estimated as the geometric mean of the constituents. The dominant minerals of the matrix, and their respective thermal conductivities (from Brigaud and Vasseur, 1989) are mica and

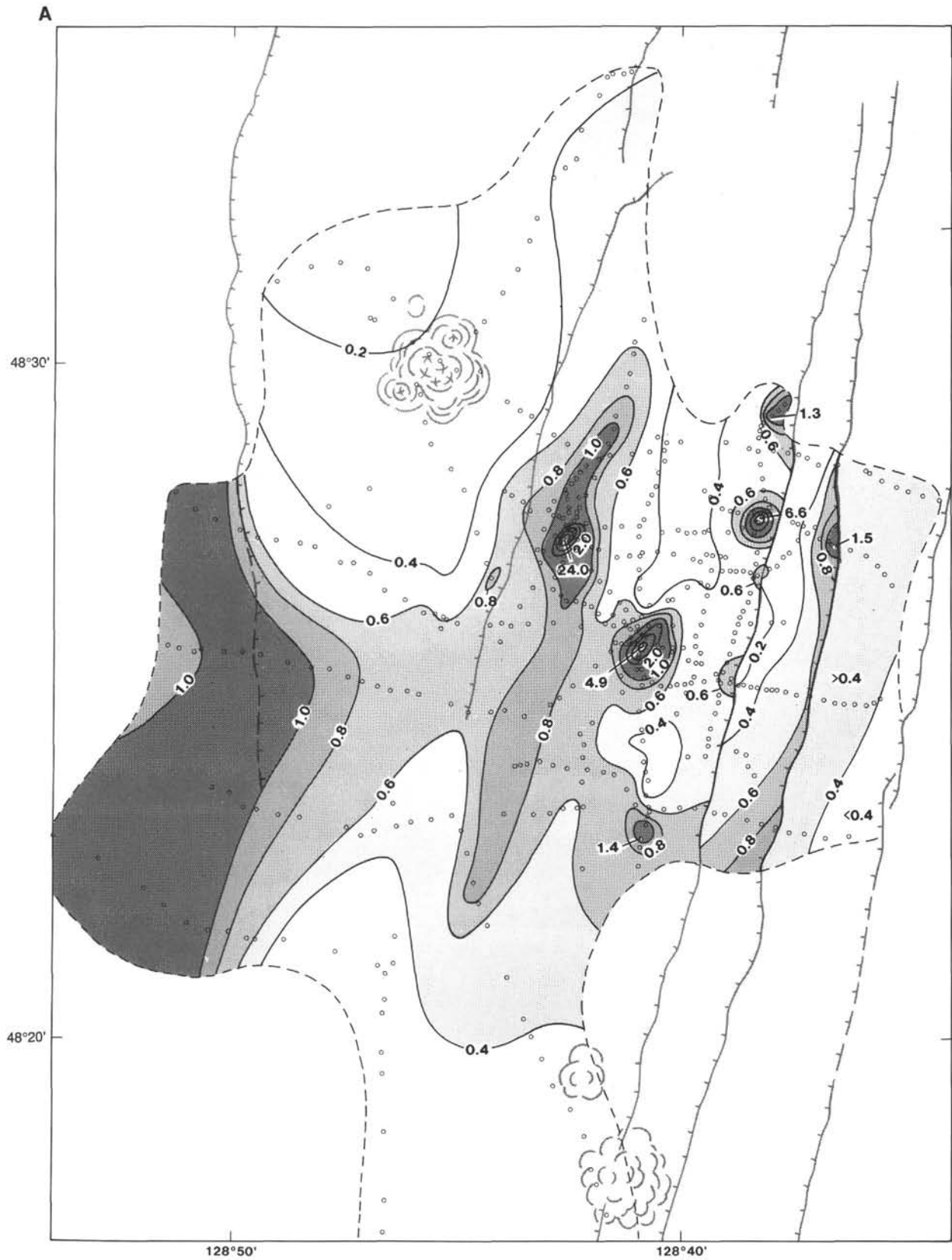


Figure 9. **A.** Heat flow in Middle Valley, hand-contoured at intervals of 0.2 W/m^2 in areas of relatively low heat flow ($<1.0 \text{ W/m}^2$) and 2.0 W/m^2 where heat flow is higher. All values are correctly represented by contours with the exception of a few isolated low values that are suspected to be erroneous. Locations of measurements are shown as open circles. The area included in the diagram is the same as that shown in (B), (C), and Figure 4. **B.** Depths (in meters) to acoustic basement, derived from the two-way travelt ime thickness of sediment estimated from seismic reflection profiles (tracklines are shown on the figure), and from the velocity-depth function given in Figure 10. **C.** Temperatures (in degrees Celsius) of the basement surface shown in (B), estimated from the heat flow distribution shown in (A), and the estimated thermal conductivity function given in Figure 12.

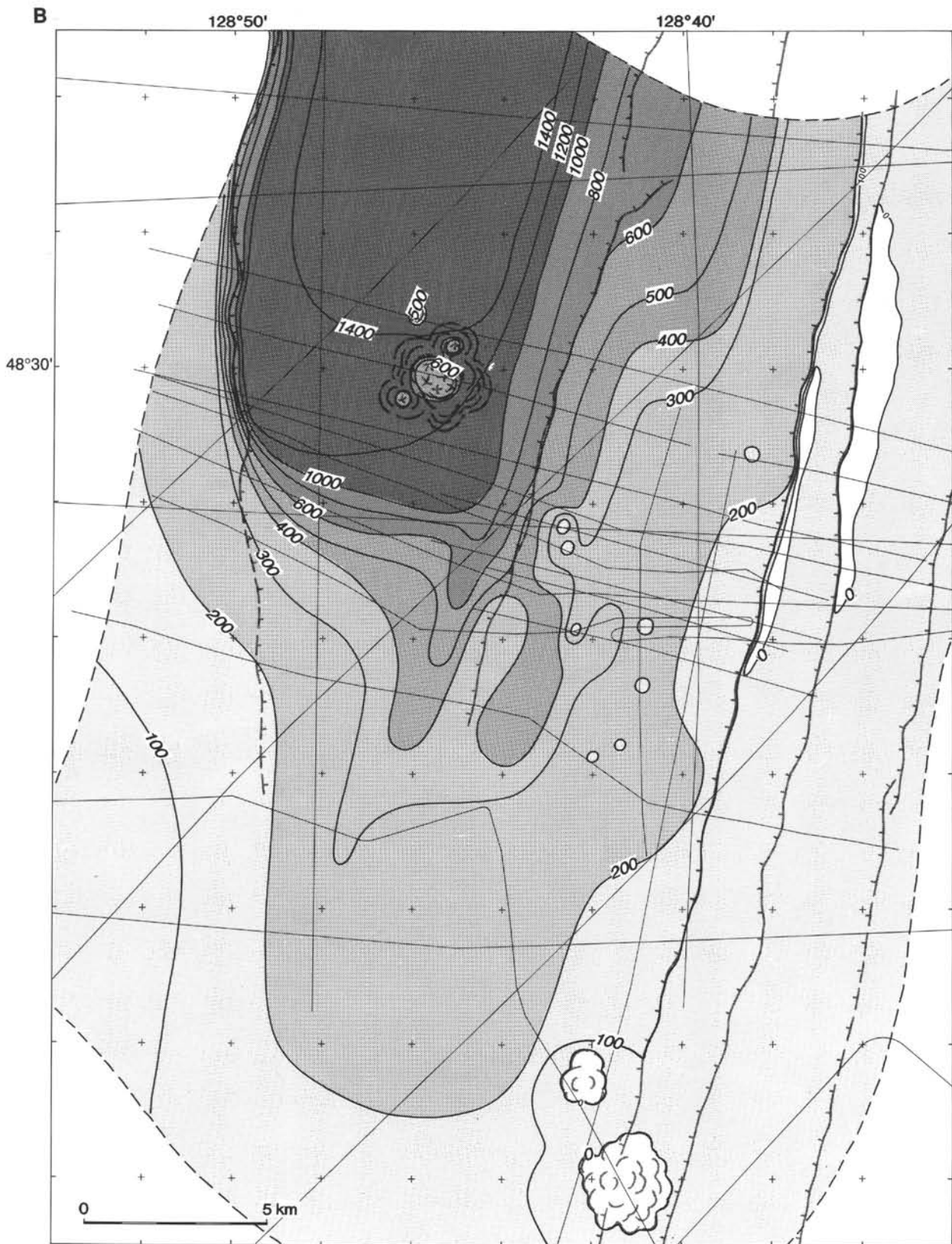


Figure 9 (continued).

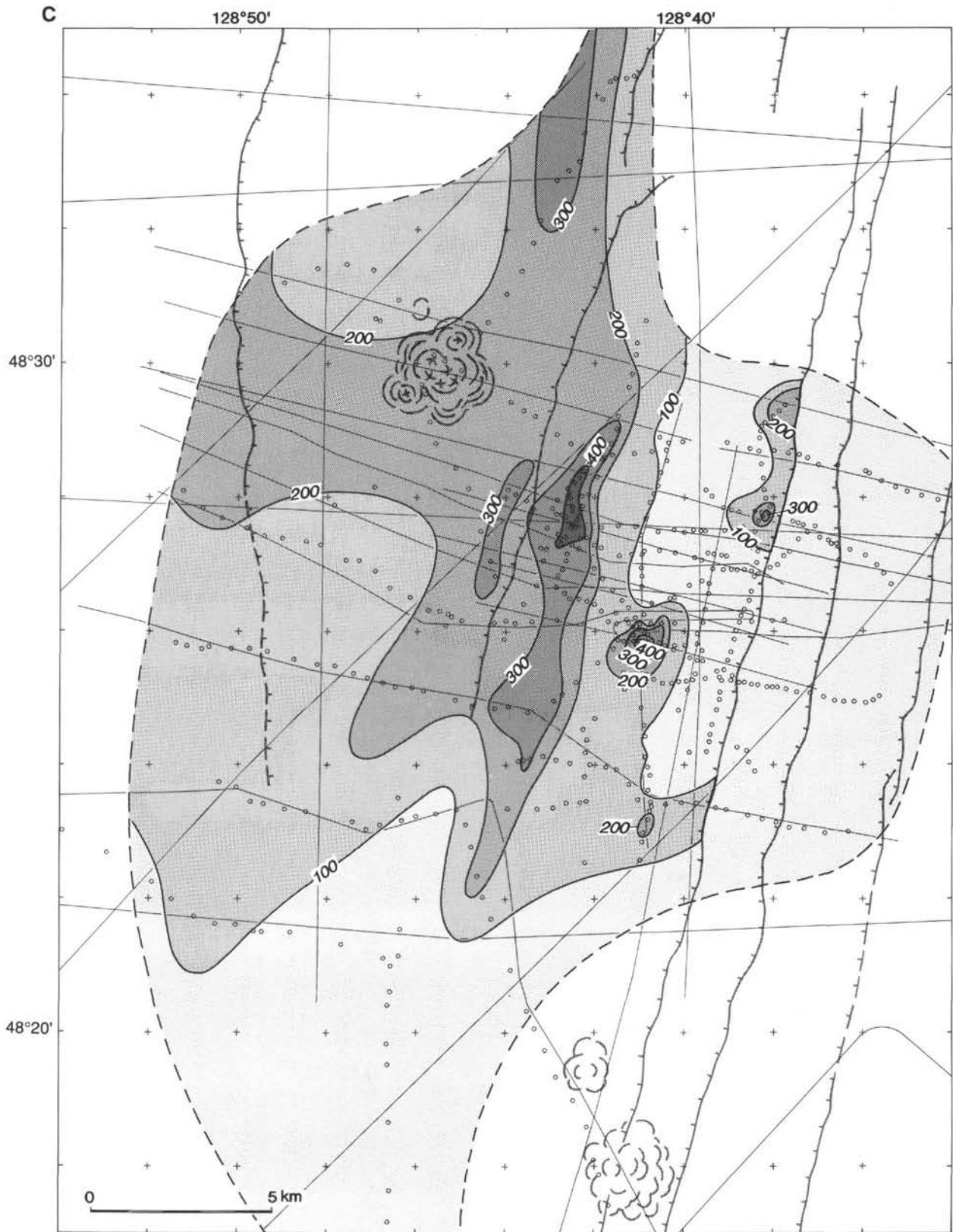


Figure 9 (continued).

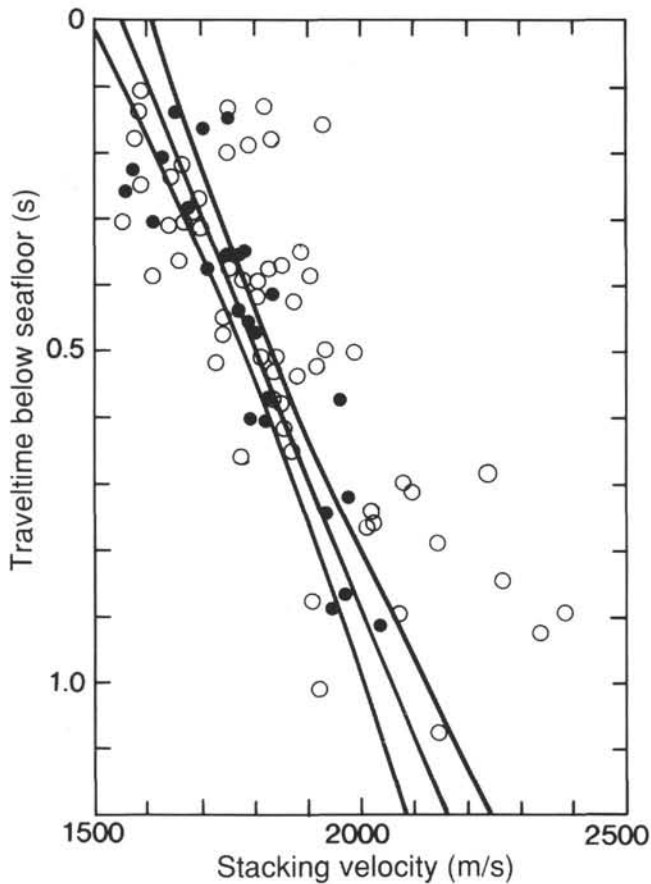


Figure 10. Average seismic velocities from the seafloor to depth, plotted against two-way traveltime, derived from semblance analyses of reflections from strong reflectors along multichannel seismic lines 89-12, -13, and -14 (Fig. 3) (open circles), and along a line crossing Cascadia Basin on the east flank of the ridge (solid circles). The regression line, shown with 95% confidence limits, is fitted through the Cascadia Basin data.

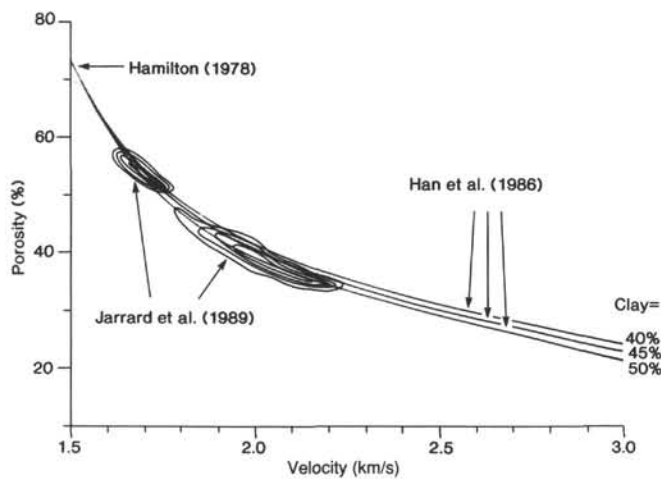


Figure 11. The velocity-porosity relationship used in this chapter to estimate the thermal conductivity at depth in Middle Valley sediments. Constraints on the relationship are provided by the references shown. An average clay content of 45% was assumed for Middle Valley, to match that estimated for Cascadia Basin by Zemmels and Cook (1973).

clay minerals ($k = 1.9 \text{ W}/[\text{m}\cdot\text{K}]$), quartz ($k = 7.7 \text{ W}/[\text{m}\cdot\text{K}]$), feldspar ($k = 2.4 \text{ W}/[\text{m}\cdot\text{K}]$), chlorite ($k = 3.3 \text{ W}/[\text{m}\cdot\text{K}]$), calcite ($k = 3.3 \text{ W}/[\text{m}\cdot\text{K}]$), and dolomite ($k = 5.3 \text{ W}/[\text{m}\cdot\text{K}]$). Assuming the average mineralogy for the Middle Valley sediments to be the same as that at DSDP Site 174 (45% mica and clay minerals, 25% quartz, 20% feldspar, 4% chlorite, 4% calcite, and 2% dolomite; Zemmels and Cook, 1973) gives an effective grain conductivity of about $3.0 \text{ W}/[\text{m}\cdot\text{K}]$. The conductivity of the sediment at a given porosity is estimated as the geometric mean of the grain and pore-fluid ($k = 0.6 \text{ W}/[\text{m}\cdot\text{K}]$) constituents. Corrections to the resulting values should be applied to account for the effects of temperature, pressure, and anisotropy in the formation. The effects of pressure are relatively small, and as the effects of temperature on the conductivity of the solid and fluid components oppose one another, the total effect of temperature is probably small as well (Clark, 1966, and references therein). The largest and, unfortunately, least quantifiable effect probably results from grain and bedding anisotropy. In shales, the ratio between the conductivities in the horizontal and vertical directions may be as high as 1.5 (see discussion in Della Vedova and Von Herzen, 1987). The grain conductivities given above were determined for fairly isotropic mixtures of rock and mineral fragments, and provide an upper limit on the value that should be used for the vertical component of the matrix conductivity in Middle Valley. To allow for the anisotropy that may be present in this section, a value for the effective mean grain conductivity 10% lower than the value given above (i.e., $2.7 \text{ W}/[\text{m}\cdot\text{K}]$) was used for the calculation of the sediment conductivity. The resulting conductivity-depth function is shown in Figure 12C, along with a temperature-depth profile that would occur in the case of a heat flow of $0.5 \text{ W}/\text{m}^2$.

Inferred Deep Thermal Structure

With the velocity and thermal conductivity profiles derived above, the thermal structure at depth in the valley can be estimated from the seafloor heat flow measurements. This is done here in two different ways. In the first case, temperatures are estimated at the base of the sediment section as defined by the isopach map in Figure 9B; these are shown in Figure 9C. Temperatures estimated for this surface, which is one estimate for the top of the permeable basement, generally fall in the range of 100° – 300°C . The lowest values (80° – 100°C) occur along the eastern part of the valley and along the fault blocks east of the rift axis. Low values are also seen in the deepest part of the rift ($<200^{\circ}\text{C}$). Estimated basement temperatures are highest in the uplifted block just east of the eastern major rift-bounding normal fault, and at other isolated locations in the eastern part of the valley where hydrothermal discharge is known or believed to occur.

Basement temperature estimates shown in Figure 9C are subject to errors arising from several sources. In the areas where hydrothermal discharge occurs, both nonvertical heat conduction, and particularly advective heat transport, can affect the thermal field significantly. This is probably true for all of the areas having locally anomalous heat flow of greater than about $1 \text{ W}/\text{m}^2$. Focused discharge is known to occur at two of these sites (J. Franklin, pers. comm., 1991; "Site 856" and "Site 858" chapters, this volume), and diffuse vertical pore fluid flow is inferred to occur on the basis of anomalous pore fluid compositions (J. Lydon, pers. comm., 1991). Rates of diffuse flow are poorly constrained by those data. The heat flow data establish an upper limit on flow by the uniformity of heat flow over the depth interval penetrated by the heat flow probe. This is demonstrated in Figure 8. There, temperature-depth profiles typical for a variety of heat flow values ranging up to nearly $8 \text{ W}/\text{m}^2$ are seen to be very linear. In Figure 8F, the perturbations to a conductive heat flow profile that would be produced by various rates of vertical pore fluid advection are shown. Given the value of thermal diffusivity of marine sediment (roughly $0.2 \times 10^{-6} \text{ m}^2/\text{s}$), the effects of reasonable rates of fluid flow on the near surface thermal profile are relatively small, and thus the sensitivity of the thermal measurements to fluid flow is low.

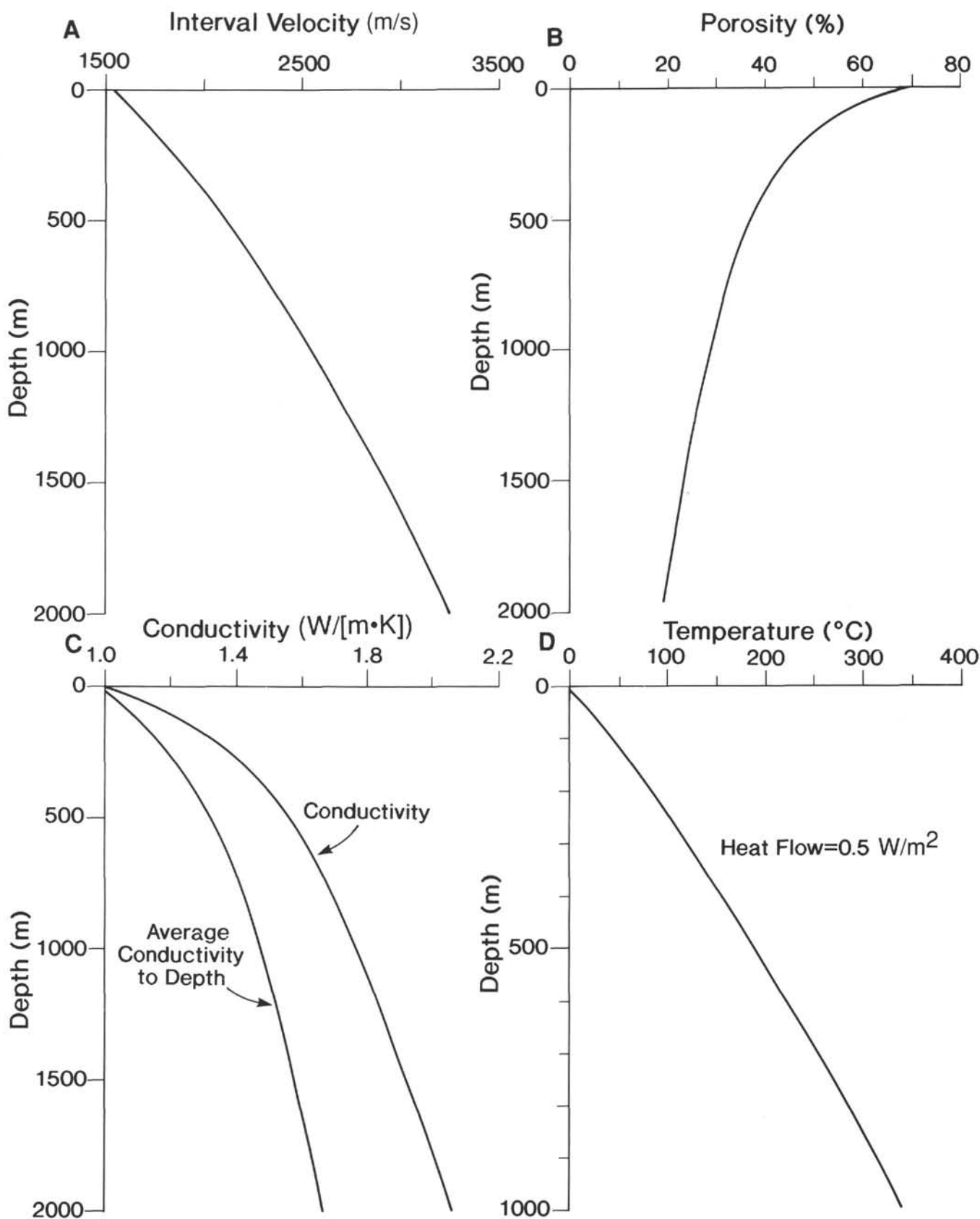


Figure 12. Physical properties estimates for the sediment section in Middle Valley, plotted against depth. **A.** Interval velocity, derived from the linear fit to the average velocity vs. travelttime data shown in Figure 10. **B.** Porosity, derived from (A) and Figure 11. **C.** Thermal conductivity, derived using a geometric mean of the constituents as outlined in the text, and the porosity function shown in Figure (B). **D.** Temperature plotted against depth, assuming the conductivity function shown in (C) for the case of a heat flow equal to 0.5 W/m².

A limit of about 0.3 m/yr is implied by the linearity of the plots of temperature vs. integrated thermal resistance (Bullard depth).

Where sediments are sufficiently thick and accumulation rates high, the surface heat flow may be reduced significantly; ignoring transient thermal conditions will cause temperatures at depth to be underestimated. A simple model has been considered by Wang and Davis (in press), who have estimated the effects of sedimentation with a simple numerical model that simulates the accumulation of a continually consolidating sediment section above a permeable basement maintained at a constant temperature by vigorous hydrothermal circulation. Although the rate of deposition in the valley is extremely high compared to rates in most seafloor environments, the combination of the efficiency of hydrothermal heat transport to the base of the sediment section, and the thermal recovery that has taken place during the post-Pleistocene period of nondeposition results in the sediment section being in a thermal state that is probably very close to steady state in most parts of the valley. The results of the model demonstrate, however, that where the sediment thickness exceeds about 1 km (see Figs. 9 and 13, line 89-12) the surface heat flow may be reduced significantly, and temperatures estimated by extrapolating surface heat flow measurements may be erroneously low.

In many parts of the valley, there may be large errors associated with the estimate of sediment thickness overlying permeable basement, and in particular, estimates derived from single-channel data may be systematically low. Correspondingly, temperatures estimated for this surface will provide systematically low estimates for the temperature of true permeable basement. To avoid the interpretive step of choosing the depth to permeable basement to be the local depth to acoustic basement, a different approach is taken in Figure 13, where temperatures at depth are shown as isotherms superimposed on seismic profiles (lines 89-12, 89-13, 89-14, and 85-03). Here the ambiguity of the sediment-basement interface is well demonstrated. In many instances, the shallowest strong reflections picked as basement for the isopach map in Figure 9B can be seen to lie several tenths of a second (several hundred meters) above deeper coherent reflective horizons, where temperatures are correspondingly higher, commonly 300°C and above. This is particularly evident in the central part of the rift along lines 89-12 and 89-14, and in the eastern part of the valley along lines 89-12 and 89-13 (Fig. 13). Thus, although not conclusive, it can be argued that the depths to acoustic basement shown in Figure 9B are erroneously shallow as estimates of depths to permeable basement, that a considerable additional thickness of sediment interbedded with basalt flows and/or sills lies beneath this level, and that the depth to permeable basement may be better estimated from the thermal rather than the seismic data.

Influence of Normal Faults

Several transects of measurements were completed across the eastern valley-bounding and adjacent normal-fault scarps (Fig. 14). Basement temperatures estimated in this part of the valley are anomalously low (Figs. 9C and 13), suggesting that the fault exposures of basement may provide pathways through which basement fluids and seawater can be exchanged efficiently. In general, the local effects of the faults on the thermal regime are not large. Along most transects, heat flow values determined in the hanging- and foot-wall blocks are generally very similar. Along two of the profiles the heat flow decreases slightly across the fault from the hanging wall to the foot wall, then increases slightly with distance from the scarp eastward across the more westerly of the two foot-wall blocks (Fig. 14); this could be caused by fluid seepage into the fault scarp and slow flow along the back-tilted permeable basement layer. Where measurements were made close to the fault scarp, both slightly elevated and depressed heat flow was observed, suggesting that both discharge and recharge may occur along the scarp. Two high-amplitude heat flow anomalies occur in the hanging-wall blocks (near 48° 27.5' N; Fig. 14), but these are well away from the adjacent fault scarps (200–500 m), and may

not be associated with flow directed by the fault. Unfortunately, navigational uncertainties and caution used when the measurements were made do not allow the detailed heat flow variations associated with the steeply dipping sediment/basement fault interface to be determined. Variations at this scale (tens of meters from the scarp) should be very sensitive to fluid flow into or out of the section.

Localized Fluid Discharge

Particularly detailed arrays of measurements were made in the vicinity of three of the areas of anomalously high heat flow. Two of the anomalies are associated with known hydrothermal discharge and mineralization at the seafloor. They are illustrated in map view in Figure 15 where heat flow values are superimposed on the local seafloor morphology, and as heat flow transects in Figure 16.

One of the anomalies is centered about 500 m south of the center of one of the uplifted hills in the eastern part of the valley, known as Bent Hill (Figs. 4, 6B, 6C, and 15A). Near the peak of the anomaly there is a small edifice (48° 25.85' N, Fig. 15A) that rises a few tens of meters above the surrounding seafloor, where sulfide rocks and debris have been observed in outcrop, and 265°C water vents through the seafloor (W. Goodfellow and R. Zierenberg, pers. comm., 1991; "Site 856" chapter, this volume). Heat flow decreases smoothly in all directions from the peak at about 5 W/m² to the local "background" level of 0.5–0.6 W/m² over a distance of several hundred meters (Figs. 15A, 16A, and 16B). No thermal anomaly associated specifically with Bent Hill can be distinguished, and it can be concluded that the age of the intrusion that uplifted the sediment section and created the topography of the hill is great enough for the thermal anomaly produced by it to have fully dissipated (i.e., a few thousand years). The same can be said about the age of the hydrothermal venting that produced the sulfide mineralization found immediately south of Bent Hill (at 48° 26.05' N, Fig. 15A). In contrast the hydrothermalism now active at the center of the heat flow anomaly must have been active for a substantial period of time for the anomaly to be as well developed as it is.

The other major thermal anomaly is centered on what is referred to as the Dead Dog hydrothermal vent field, where fluids discharge through the seafloor at vents scattered over an area roughly 250 by 700 m in dimension at temperatures typically between 255° and 275° C (J. Franklin, pers. comm., 1991; "Site 858" chapter, this volume). The vent field is characterized by acoustically rough seafloor (Fig. 15B) that is locally depressed by about 10 m (Fig. 6D). The field is underlain by a buried basement edifice (Fig. 6D) at about 160 ms TWT below the seafloor. Heat flow measured within and in the immediate vicinity of the field is shown in Figures 15B, 16C, and 16D. Values within the field are high, most greater than 4 W/m², and variable, ranging up to 25 W/m². Unfortunately, given the uncertainty in the location of the measurements of typically 100 m, the details of the variability cannot be resolved. Heat flow in the area surrounding the vent field decreases systematically with distance from the field, as can be seen clearly in the transects shown in Figure 16C, 16D. As in the case of the anomaly south of Bent Hill, the heat flow falls to background levels over a distance a few hundred meters along the east-west transect.

Implications for Fluid Flow

No attempt to model quantitatively the fluid flow regime responsible for the heat flow variations in Middle Valley is made here. This will be done once the strong additional constraints provided by the drilling leg are available, as discussed above. In the most general terms the situation defined by the combination of the thermal structure and inferred permeability structure of the valley can probably be explained by a model in which fluids reside in a permeable upper crustal "reservoir" and "leak" through a generally continuous and low-permeability sediment cover at isolated locations where base-

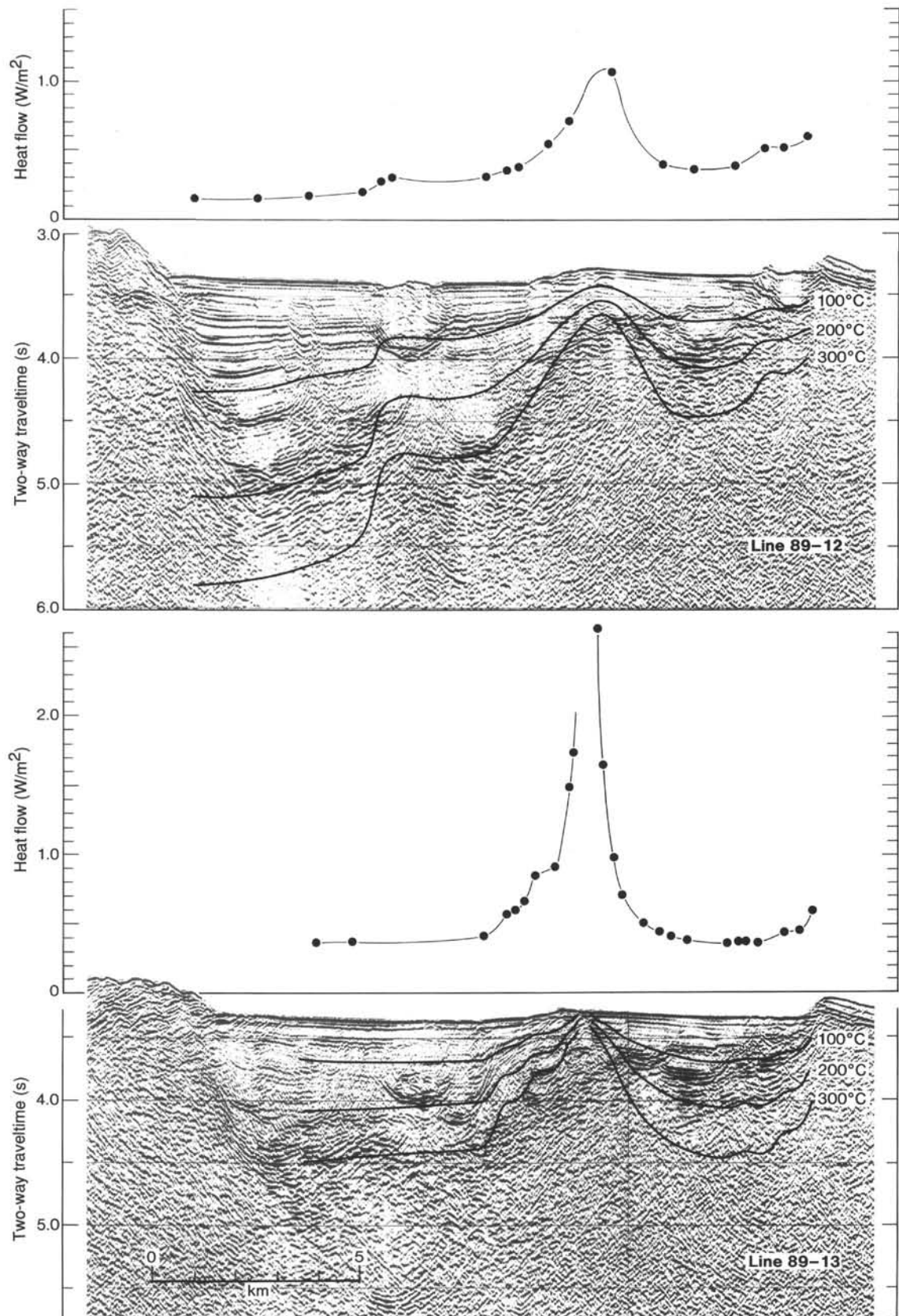


Figure 13. Seismic profiles with heat flow values, measured within a few hundred meters, projected onto the lines. Temperatures at depth (shown as two-way traveltime), estimated from the heat flow and the physical properties given in Figures 10 and 12, are shown as isotherms superimposed on the profiles.

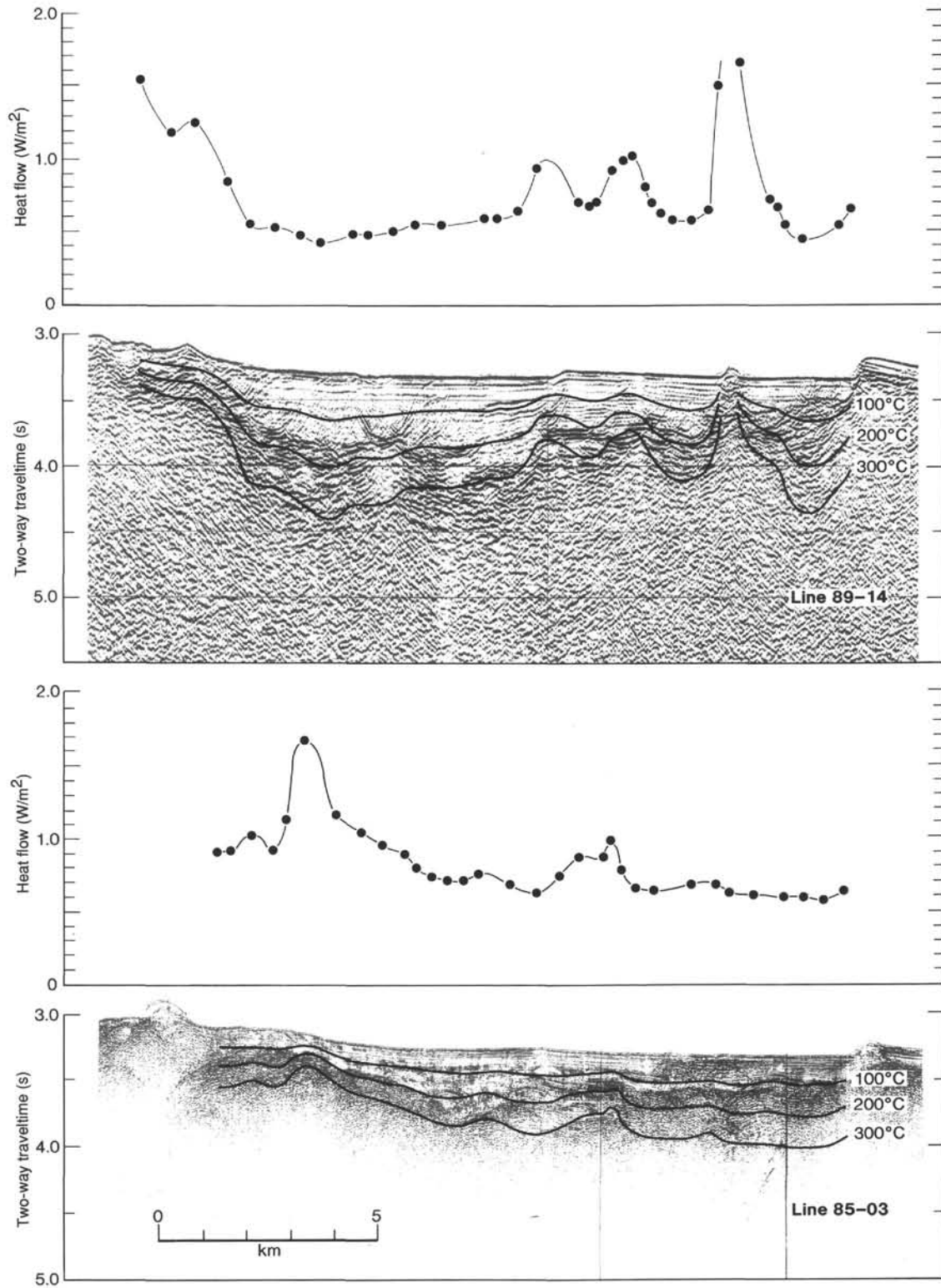


Figure 13 (continued).

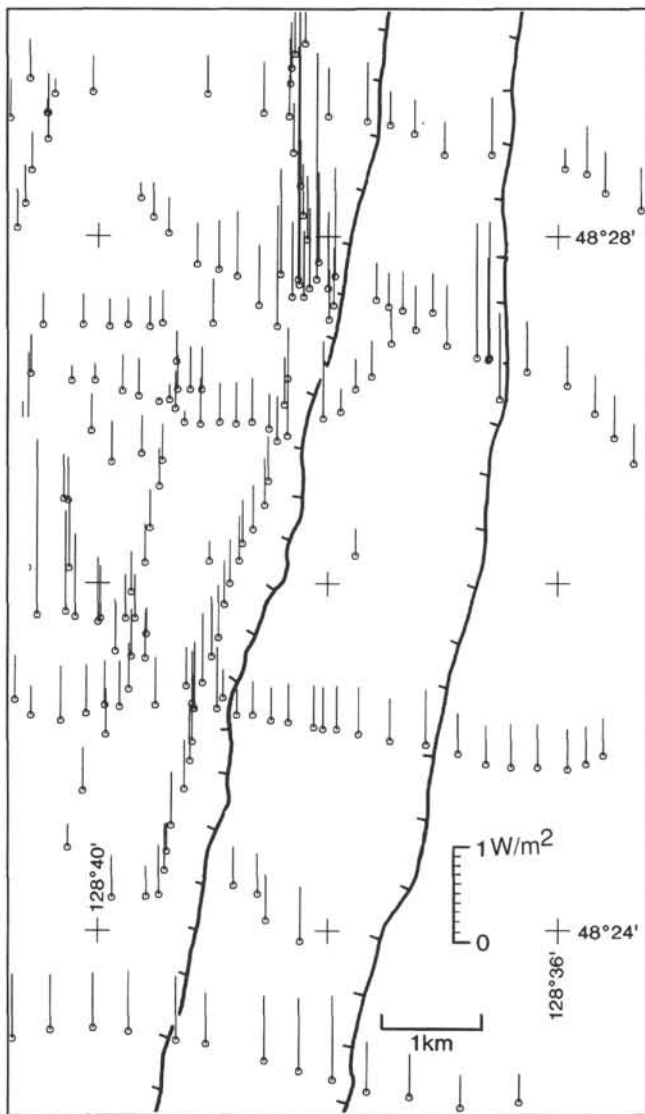


Figure 14. Heat flow variations in the vicinity of the normal faults that expose basement along the eastern side of Middle Valley.

ment or other permeable conduits breach the sediment. This model has been suggested to explain observations in a sedimented ridge flank setting of Cascadia Basin (Davis et al., 1989, in press) and would seem to be applicable in Middle Valley, given the generally uniform inferred temperatures in permeable basement and the association between hydrothermal discharge zones and thinly buried basement (e.g., Figs. 9 and 13).

In the areas of discharge, the anomalous seafloor heat flow is probably the result of both conductive and advective effects. Diffuse vertical fluid flow through the sediment section at a rate high enough to contribute to the surface conductive heat flow, but too low to be detected in the typically 2- to 4-m-deep measurements themselves is undoubtedly important (see Fig. 8F). Anomalous heat flow must also be in part a conductive result of sediment thickness variations above a roughly constant-temperature hydrothermal reservoir, just as in the case proposed for the regional variations. A third possibility is that the anomalous heat flow is due to the lateral conduction of heat and advection through permeable layers away from discrete vertical feeder zones located directly beneath the vents themselves. Hypothetical geotherms resulting from the first two of these mechanisms are illustrated in Figure 17. In reality, some combination of all of these

processes is likely to be the cause of the heat flow variations observed. The relative importance of each cannot be determined from the existing seafloor data, although additional constraints will be provided by drilling results, and by pore fluid geochemical profiles determined from cores collected from one of the areas of venting (J. Lydon, pers. comm., 1991).

It is interesting to note that, while the exit temperatures from the vents in the valley are very consistent with those estimated for permeable basement, neither are high enough to create the highly reduced fluids and attendant high concentrations of dissolved metals necessary for massive sulfide mineral deposition. The presence of the sulfide deposits in the valley (e.g., Davis, Goodfellow, et al., 1987; J. Franklin and W. Goodfellow, pers. comm., 1991) requires that such fluids have been produced, and thus different thermal conditions in the past are implied. Two explanations for this temporal variability are reasonable. The deposits may have been produced in special circumstances, when a local heat source was being tapped directly beneath a discharge point. It is also possible that temperatures of the entire reservoir rise and fall according to the balance of heat at any given time between sources located anywhere beneath the sediment fill of the valley and the combined conductive and advective heat loss through the valley floor. That temperatures could be occasionally higher is suggested by the amount of heat supplied by the solidifying and cooling to 300°C of a several-kilometer-thick crustal layer. Assuming the crustal age to range from 0 to 400,000 yr (Fig. 3), the spreading rate to be 60 mm/yr, and the solidified and cooled crust to be 5 km thick, an average heat dissipation of roughly 3.5 W/m² is required. This is clearly larger than the average conductive heat loss through the valley floor at present (Fig. 9A), indicating that higher basement temperatures could be supported.

SUMMARY

A suite of closely spaced heat flow measurements in Middle Valley, northern Juan de Fuca Ridge, combined with seismic reflection profiles and previously published bathymetric and acoustic image data, lead to several conclusions about the tectonic history and hydrologic structure of this sediment-filled seafloor spreading rift, and about hydrothermal processes in such settings in general.

1. While the Juan de Fuca Ridge is in general volcanically "robust," the north end of the ridge appears to be "starved"; spreading takes place in three deep axial rift valleys. It is inferred that this is a result of the effects of the cooler conditions that normally exist at ridge-transform intersections, and of the northward migration of the ridge in the wake of the Explorer plate.

2. The igneous crust of the primary rift in the area, Middle Valley, is buried by a continuous fill of turbidite sediment along its entire length. Heat flow in the valley is inversely correlated with sediment thickness; this is consistent with a model in which hydrothermal circulation maintains relatively uniform temperatures in the upper igneous crust beneath a seal of relatively low-permeability sediments.

3. Numerous local heat flow anomalies occur in the valley. In two instances these are known to be associated with discharge of hydrothermal fluids at the seafloor at temperatures roughly the same as that estimated for the top of permeable basement in the surrounding region. At these sites, the anomalies and the associated vents or vent fields are underlain by buried basement edifices. It is inferred that the local permeable pathways created by these edifices and the attenuated sections of sediment that cover them exert a strong control on the location of hydrothermal upflow and discharge.

4. A local intrusion disrupts the Holocene sediment surface in the center of the rift valley. There is a small heat flow anomaly associated with this intrusion, although there appears to be no associated hydrothermal activity. The sediment section at this location, even though structurally disrupted, still serves as a hydrologic seal, and prevents hydrothermal discharge from occurring above this local heat source.

5. The temperatures in the hydrothermal "reservoir" that underlies the sediment fill in Middle Valley (ca. 300°C) are not sufficiently high to generate "ore-forming fluids" (>380°C). The sulfide deposits observed in the valley require either special local conditions, or temporal variations in heat supply that occasionally raise the reservoir temperature.

ACKNOWLEDGMENTS

Many individuals were involved in the collection and processing of the data from the various cruises on which this paper is based. W. Bentkowski assisted at sea during many of the cruises and helped with the reduction of the heat flow measurements. R. Currie helped with navigation and produced the magnetic anomaly map. M. Bone played a key role in the design, operation, and maintenance of two generations of heat flow probes used in the course of the work. The captains and crews of the CSS *Parizeau* and the CSS *Tully* provided able assistance in handling equipment through all kinds of weather and their ships during tedious station keeping. The multichannel seismic reflection data were collected by Digicon, Inc., and processed by Haliburton Geophysical Services, with technical assistance from K. Rohr, R. Hyndman, and G. Spence. Although most of the bathymetric and side-scan data have been published previously, W. Ryan, D. Hussong, S. Hammond, R. Currie, M. Williamson, P. Johnson, B. Sawyer, and many others are to be thanked for their contributions to that work. R. Franklin prepared most of the figures. One of the authors' (H.V.) participation in the heat flow cruises was made possible by a NSERC Visiting Fellowship (1983–1985) and later by travel grants from the German-Canadian Agreement on the Exchange of Science and Technology. GSC contribution number 10492.

REFERENCES

- Abbott, D. H., Morton, J. L., and Holmes, M. L., 1986. Heat-flow measurements on a hydrothermally active, slow-spreading ridge: the Escanaba Trough. *Geophys. Res. Lett.*, 13:678–680.
- Al-Aasm, I. S., and Blaise, B., 1991. Interaction between hemipelagic sediment and a hydrothermal system: Middle Valley, northern Juan de Fuca Ridge, subarctic northeast Pacific. *Mar. Geol.*, 98:25–40.
- Barr, S. M., and Chase, R. L., 1974. Geology of the northern end of Juan de Fuca Ridge and seafloor spreading. *Can. J. Earth Sci.*, 11:1384–1406.
- Becker, K., and Fisher, A. T., 1991. A brief review of heat-flow studies in the Guaymas Basin, Gulf of California. In Dauphin, J. P., and Simoneit, B.R.T. (Eds.), *The Gulf and Peninsular Province of the Californias*. AAPG Mem., 47.
- Bredehoeft, J. D., and Papadopoulos, I. S., 1965. Rates of vertical groundwater movement estimated from the earth's thermal profile. *Water Resour. Res.*, 1:325–328.
- Brigaud, F., and Vasseur, G., 1989. Mineralogy, porosity and fluid control on thermal conductivity of sedimentary rocks. *Geophys. J.*, 98:525–542.
- Clark, S. P., 1966. Thermal conductivity. In Clark, S. P. (Ed.), *Handbook of Physical Constants*. Mem.–Geol. Soc. Am., 97:461–482.
- Cowan, D. S., Botros, M., and Johnson, H. P., 1986. Bookshelf tectonics: Rotated crustal blocks within the Sovanco fracture zone. *Geophys. Res. Lett.*, 13:995–998.
- Crane, K., Aikman, F., Embley, R., Hammond, S., Malahoff, A., and Lupton, J., 1985. The distribution of geothermal fields on the Juan de Fuca Ridge. *J. Geophys. Res.*, 90:727–744.
- Currie, R. G., Cooper, R. V., Riddihough, R. P., and Seemann, D. A., 1983. Multiparameter geophysical surveys off the west coast of Canada: 1973–1982. In *Current Research* (Pt. A). Geol. Surv. Can., Pap. 83–1A:202–212.
- Currie, R. G., Davis, E. E., Riddihough, R. P., and Sawyer, B. S., 1985. Juan de Fuca Ridge Atlas: preliminary Sea Beam Bathymetry. Geol. Surv. Can., Open File, 1143.
- Davis, E. E., and Becker, K., 1992. Thermal and tectonic structure of the Escanaba Trough: new heat-flow measurements and seismic-reflection profiles. In Morton, J., Zierenberg, R., and Reiss, C. A. (Eds.), *Geologic, Hydrothermal and Biological Studies at Escanaba Trough, Gorda Ridge, Offshore California*. USGS Bull., 2022.
- Davis, E. E., Chapman, D. S., Forster, C. B., and Villinger, H., 1989. Heat-flow variations correlated with buried basement topography on the Juan de Fuca Ridge flank. *Nature*, 342:533–537.
- Davis, E. E., Chapman, D. S., Mottl, M. J., Bentkowski, W., Dadey, K., Forster, C., Harris, R., Nagihara, S., Rohr, K., Wheat, G., and Whitticar, M., in press. FlankFlux: an experiment to study the nature of hydrothermal circulation in young oceanic crust. *Can. J. Earth Sci.*
- Davis, E. E., Currie, R. G., and Kosalos, J. G., 1986. The use of swath bathymetric and acoustic image mapping tools in marine geoscience. *Mar. Tech. Soc. J.*, 20:17–21.
- Davis, E. E., Currie, R. G., and Sawyer, B. S., 1987. Marine geophysical maps of western Canada: regional SeaMARC II acoustic image mosaics and Sea Beam bathymetry. *Geol. Surv. Can.*, Maps 2-1987-17-1987.
- Davis, E. E., Currie, R. G., Sawyer, B. S., and Hussong, D. M., 1984. Juan de Fuca Ridge Atlas: SeaMARC II acoustic imagery. *Earth Phys. Branch, Energy Mines Resour. Can., Open File*, 84-17.
- Davis, E. E., Goodfellow, W. D., Bornhold, B. D., Adshead, J., Blaise, B., Villinger, H., and Le Cheminant, G. M., 1987. Massive sulfides in a sedimented rift valley, northern Juan de Fuca Ridge. *Earth Planet. Sci. Lett.*, 82:49–61.
- Davis, E. E., and Lister, C.R.B., 1977a. Heat flow measured over the Juan de Fuca Ridge: evidence for widespread hydrothermal circulation in a highly heat-transportive crust. *J. Geophys. Res.*, 82:7845–4860.
- , 1977b. Tectonic structures on the Juan de Fuca Ridge. *Geol. Soc. Am. Bull.*, 88:346–363.
- Della Vedova, B., and Von Herzen, R. P., 1987. Geothermal heat flux at the COST B-2 wells, U.S. Atlantic continental margin. *WHOI Tech. Rep.*, 87-28.
- Dellinger, P., and Holmes, M. L., 1992. Thermal and mechanical models for sediment hills and associated sulfide deposits along the Escanaba Trough. In Morton, J. L., Zierenberg, R., and Reiss, C. A. (Eds.), *Geologic, Hydrothermal and Biological Studies at Escanaba Trough, Gorda Ridge, Offshore California*. U.S.G.S. Bull., 2022.
- Fisher, A. T., and Becker, K., in press. Heat flow, hydrothermal circulation, and basalt intrusions in the Guaymas Basin, Gulf of California. *Earth Planet. Sci. Lett.*
- Fisher, A. T., Becker, K., Narasimhan, T. N., Langseth, M. G., and Mottl, M. J., 1990. Passive, off-axis convection through the southern flank of the Costa Rica rift. *J. Geophys. Res.*, 95:9343–9370.
- Goodfellow, W. G., and Blaise, B., 1988. Sulfide formation and hydrothermal alteration of hemipelagic sediment in Middle Valley, northern Juan de Fuca Ridge. *Can. Mineral.*, 26:675–696.
- Hamilton, E. L., 1978. Sound velocity-density relations in seafloor sediments and rocks. *J. Acoust. Soc. Am.*, 63:366–377.
- Han, D., Nur, A., and Morgan, D., 1986. Effects of porosity and clay content on wave velocities in sandstones. *Geophysics*, 51:2093–2107.
- Hyndman, R. D., Davis, E. E., and Wright, J. A., 1979. The measurement of marine geothermal heat flow by a multipenetration probe with digital acoustic telemetry and *in-situ* thermal conductivity. *Mar. Geophys. Res.*, 4:181–205.
- Hyndman, R. D., Riddihough, R. P., and Herzer, R., 1979. The Nootka fault zone: a new plate boundary off western Canada. *Geophys. J.*, 58:667–683.
- Jarrard, R. D., Dadey, K. A., and Busch, W. H., 1989. Velocity and density of sediments of Eirik Ridge, Labrador Sea: control by porosity and mineralogy. In Srivastava, S. P., Arthur, M. A., Clement, B., et al., *Proc. ODP, Sci. Results*, 105: College Station, TX (Ocean Drilling Program), 811–835.
- Johnson, H. P., Franklin, J. M., and Currie, R. G., in press. SeaMARC IA acoustic imagery of the Middle Valley area, northern Juan de Fuca Ridge. *Geol. Surv. Open File*.
- Karsten, J., Hammond, S. R., Davis, E. E., and Currie, R. G., 1986. Detailed geomorphology of the Endeavour segment of the Juan de Fuca Ridge. *Geol. Soc. Am. Bull.*, 97:213–221.
- Koski, R. A., Shanks, W. C., III, Bohrsen, W. A., and Oscarson, R. L., 1988. The composition of massive sulfide deposits from the sediment-covered floor of Escanaba Trough, Gorda Ridge: implications for depositional processes. *Can. Mineral.*, 26:655–673.
- Lawver, L. A., and Williams, D., 1979. Heat flow in the central Gulf of California. *J. Geophys. Res.*, 84:3465–3478.
- Lawver, L. A., Williams, D., and Von Herzen, R. P., 1975. A major geothermal anomaly in the Gulf of California. *Nature*, 257:23–28.
- Levi, S., and Riddihough, R., 1986. Why are marine magnetic anomalies suppressed over sedimented spreading centers? *Geology*, 14:651–654.

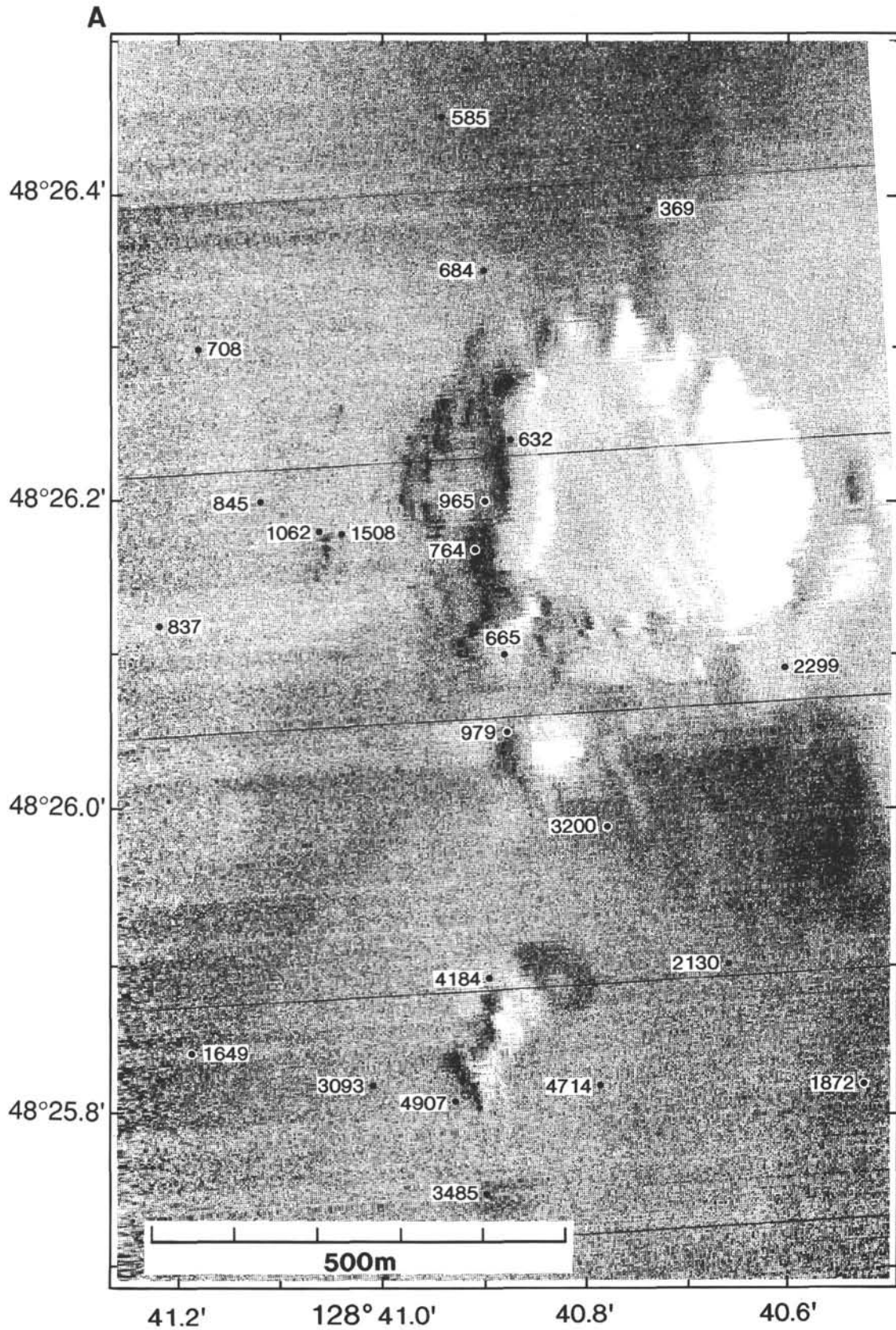


Figure 15. Heat flow determinations over and in the vicinity of the uplifted hill of sediment referred to as Bent Hill (A), and the vent field referred to as Dead Dog (B). Values are superimposed on SeaMARC IA imagery of each of the features (Johnson et al., in press). Navigational uncertainty of the acoustic imagery is less than a few tens of meters, and of the heat flow measurements roughly 100 m.

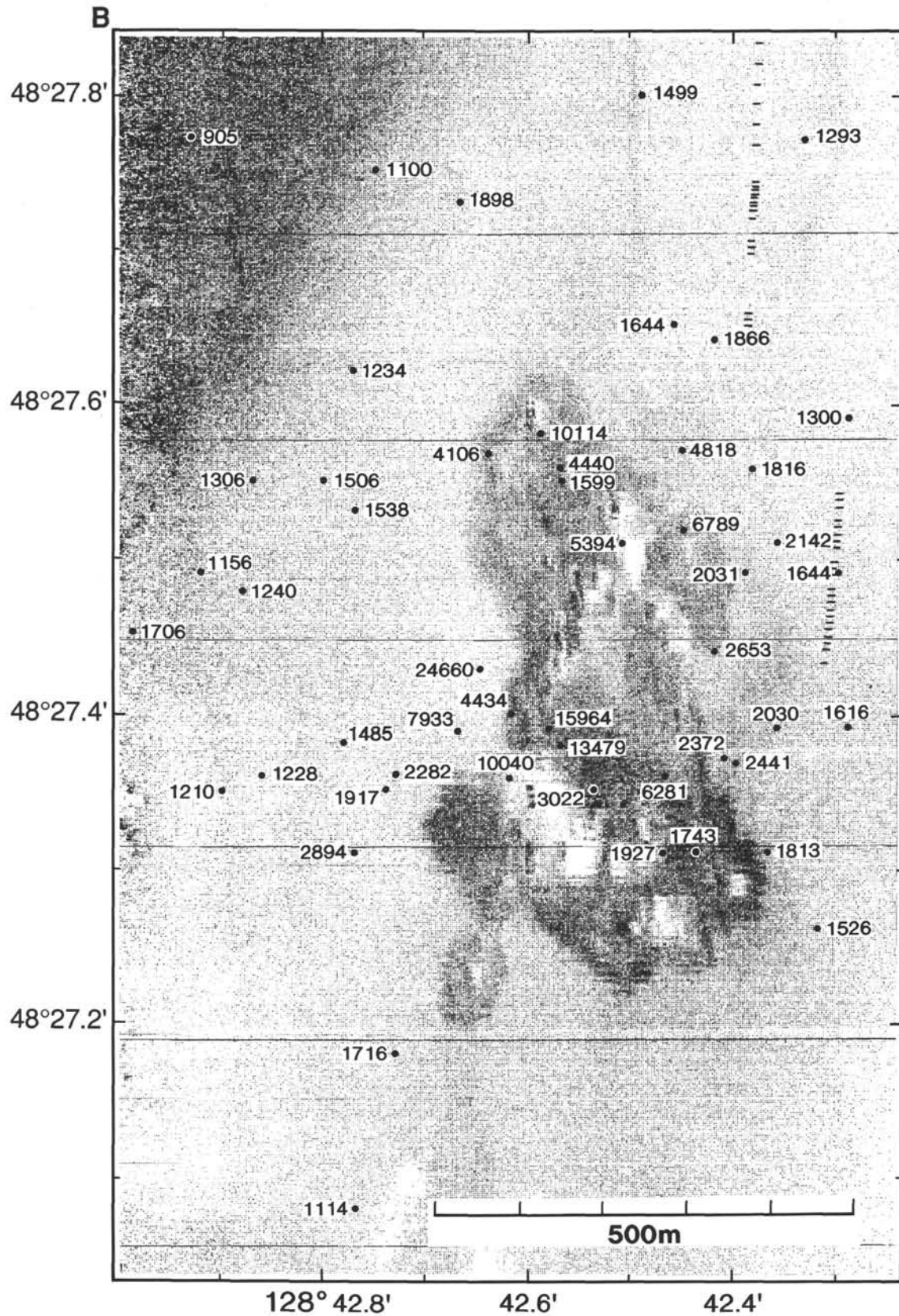


Figure 15 (continued).

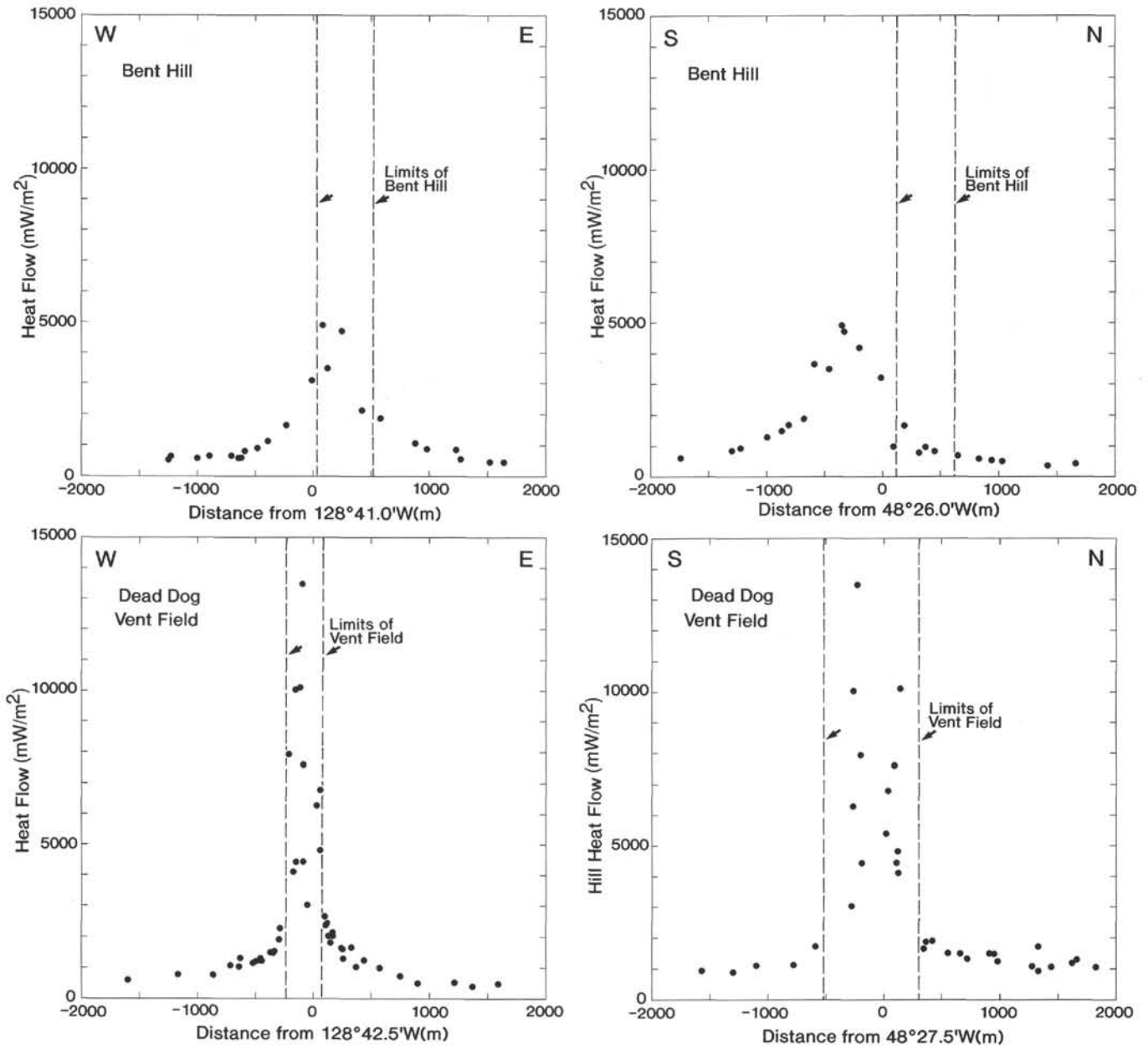


Figure 16. Profiles of heat flow through the anomalies shown in Figure 15. Measurements have been projected up to 200 m onto lines striking north-south and east-west through the peaks of the anomalies.

Lister, C.R.B., 1989. Plate tectonics at an awkward junction: rules for the evolution of Sovanco Ridge area, NE Pacific. *Geophys. J.*, 96:191-201.
 Lonsdale, P., and Becker, K., 1985. Hydrothermal plumes, hot springs, and conductive heat flow in the southern trough of Guaymas Basin. *Earth Planet. Sci. Lett.*, 73:211-225.
 Lucas, W. H., 1972. Juan de Fuca ridge and Sovanco fracture zone. *NOAA Tech. Rep.*, ERL 234-Pol 11.
 Luternauer, J. L., Conway, K. W., Clague, J. J., and Blaise, B., 1989. Late Quaternary geology and geochronology of the central continental shelf of Western Canada. *Mar. Geol.*, 89:57-68.
 McManus, D. A., Holmes, M. L., Carson, B., and Barr, S. M., 1972. Late quaternary tectonics, northern end of Juan de Fuca Ridge (northeast Pacific). *Mar. Geol.*, 12:141-164.
 Morton, J. L., Holmes, M. L., and Koski, R. A., 1987. Volcanism and massive sulfide formation at a sedimented spreading center, Escanaba Trough, Gorda Ridge, northeast Pacific Ocean. *Geophys. Res. Lett.*, 14:769-772.

Nobes, D. C., Villinger, H., Davis, E. E., and Law, L. K., 1986. The determination of resistivity and porosity of the sediment and fractured basalt layers near the Juan de Fuca Ridge. *J. Geophys. Res.*, 91:14033-14043.
 Pearson, W. C., 1975. Gravity study of the Juan de Fuca ridge and Sovanco fracture zone in the northeast Pacific [Ph.D. thesis]. Univ. of Washington, Seattle.
 Raff, A. D., and Mason, R. G., 1961. Magnetic survey off the west coast of North America 40°N latitude to 50°N latitude. *Geol. Soc. Am. Bull.*, 71:1267-1270.
 Riddihough, R. P., 1983. Recent plate motions, Juan de Fuca Plate. *Map JFP-9, Earth Phys. Branch Open File*, 83-6.
 ———, 1984. Recent movements of the Juan de Fuca plate system. *J. Geophys. Res.*, 89:6980-6994.
 Rohr, K. M., Davis, E. E., and Hyndman, R. D., 1992. Multichannel seismic reflection profiles across Middle Valley, northern Juan de Fuca Ridge. *Geol. Surv. Can. Open File*, 2476.

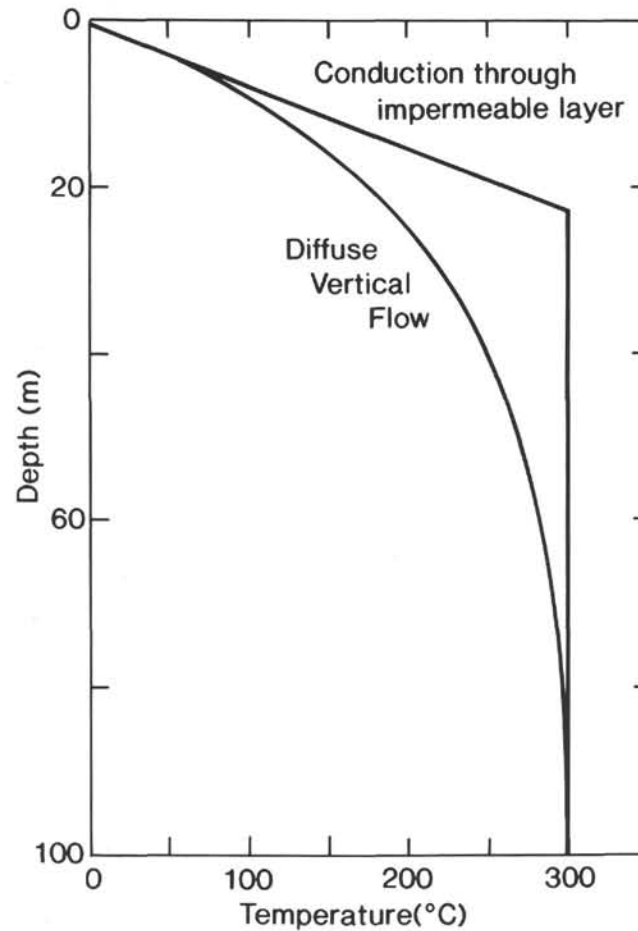


Figure 17. Hypothetical temperature-depth profiles shown for two mechanisms that could be responsible for the anomalous heat flow observed near the Dead Dog and Bent Hill vents in Middle Valley, including diffuse pore-fluid flux and an anomalously shallow high-temperature hydrothermal "reservoir" beneath impermeable sediment.

- Sleep, N. H., and Biehler, S., 1970. Topography and tectonics at the intersections of fracture zones with central rifts. *J. Geophys. Res.*, 75:2748-2752.
- Villinger, H., and Davis, E. E., 1987. A new reduction algorithm for marine heat-flow measurements. *J. Geophys. Res.*, 92:12846-12856.
- Waldstrom, R., and Rogers, G. C., 1990. Relocation of earthquakes offshore Vancouver Island. *Geol. Surv. Can. Open File*, 2288.
- Wang, K., and Davis, E., in press. Thermal effects of marine sedimentation in hydrothermally active areas. *Geophys. J.*

- Williams, D., Becker, K., Lawver, L., and Von Herzen, R., 1979. Heat flow at the spreading centers of the Guaymas Basin, Gulf of California. *J. Geophys. Res.*, 84:6757-6769.
- Zemmels, I., and Cook, H. E., 1973. X-ray mineralogy of sediments from the northeast Pacific and Gulf of Alaska-Leg 18 Deep Sea Drilling Project. In Kulm, L. D., von Huene, R., et al., *Init. Repts. DSDP*, 18: Washington (U.S. Govt. Printing Office), 1015-1060.

Ms 139A-102